



Supplementary Materials for

The structure of human CST reveals a decameric assembly bound to telomeric DNA

Ci Ji Lim, Alexandra T. Barbour, Arthur J. Zaug, Karen J. Goodrich, Allison E. McKay, Deborah S. Wuttke*, Thomas R. Cech*

*Corresponding author. Email: thomas.cech@colorado.edu (T.R.C.); deborah.wuttke@colorado.edu (D.S.W.)

Published 5 June 2020, *Science* **368**, 1081 (2020)
DOI: 10.1126/science.aaz9649

This PDF file includes:

Materials and Methods
Figs. S1 to S19
Tables S1 to S3
References

Materials and Methods

Expression and purification of CST in insect cells

Expression of the human CST complex was adapted from the previously described protocol (23), with tandem affinity purification now included. Briefly, the Multi-Bac insect cell expression system (37) was used to generate a single baculovirus that co-expresses the three CST subunits - 2xFLAG-CTC1 (Accession number: AAI11784), 6xHIS-STN1 (NP_079204) and 6xHIS-TEN1 (NP_001106795) - in *Trichoplusia ni* (Tni) cells (Expression Systems, USA). The baculovirus was amplified to a titer of at least 1.0×10^8 pfu/mL (measured by titering service, Expression Systems, USA) before using it for infection. Two to four liters of healthy Tni cells were infected at a M.O.I of 2 at a cell density of $1.5\text{-}2.0 \times 10^6$ cells/mL. The infected cells were then incubated in a shaker for 69 h at 27 °C and 130 rpm.

The cells were collected by centrifugation at 1,000 x g for 30 min at 4 °C, and the cell pellet was resuspended in lysis buffer (50 mM HEPES-NaOH pH 7.5, 300 mM NaCl, 15 mM imidazole, 1 mM TCEP, EDTA-free protease inhibitors (1 tablet per 50 mL lysis buffer, Roche, USA)) at 50 mL lysis buffer per liter of cells before undergoing sonication for cell lysis. The cell lysate was clarified by high-speed centrifugation at 35,000 x g for 45 min at 4 °C. Ni-NTA agarose resin (Qiagen, USA) pre-equilibrated with lysis buffer was then added to the clarified lysate (5 mL resin per 200 mL supernatant) under stirring condition at 4 °C. The resin was allowed to capture the 6xHIS-tagged proteins for 2 h before washing three times with wash buffer (50 mM HEPES-NaOH pH 7.5, 300 mM NaCl, 15 mM imidazole, 1 mM TCEP) prior to elution with Ni-NTA elution buffer (50 mM HEPES-NaOH pH 7.5, 300 mM NaCl, 300 mM imidazole, 1 mM TCEP, EDTA-free protease inhibitors (1 tablet per 50 mL lysis buffer, Roche, USA)). Anti-FLAG resin (GenScript, USA) pre-equilibrated with Ni-NTA elution buffer was added to the eluted proteins at 7.5 mL resin per 50 mL of elution, and allowed to capture the 2xFLAG-tagged proteins overnight on a rotator at 4 °C. The resin was washed three times with wash buffer before eluting with FLAG elution buffer (50 mM HEPES-NaOH pH 7.5, 300 mM NaCl, 15 mM imidazole, 1 mM TCEP, 0.4 mg/mL 3xFLAG peptide (APEXBIO, USA)). The integrity and purity of eluted CST was confirmed using SDS-PAGE before it was concentrated to a final protein concentration of 5.0-10.0 mg/mL. The purified CST protein was then immediately used for EM sample preparations or liquid-nitrogen snap-frozen for future biochemical work. Gel filtration analysis was done with Superose 6 increase 10/300 column (GE Healthcare Life Sciences, USA) on an FPLC system (ATKA pure, GE Life Sciences) with simultaneous detection at 280 and 260 nm.

Negative-stain electron microscopy

Purified CST complexes were negatively stained with 2 % (w/v) uranyl formate (Structure Probe, USA) using a previously described protocol (38). The protein concentration used during grid (CF400-Cu-UL, EMS, USA) preparation was optimized (~10 nM) to ensure we achieved a particle density range suitable for single-particle analysis. The negatively stained grids were imaged on a FEI TECNAI F30 300 kV transmission electron microscope (Thermo Fisher Scientific, USA) at 31,000 x ($3.216 \text{ \AA pixel}^{-1}$) magnification, total dose of 15 e-/\AA^2 and a defocus range of -0.5 to -1.5 μm . Datasets were recorded with SerialEM (39) using the Gatan 4k x 4k OneView CMOS camera (Gatan, USA). The micrograph stacks were processed with GCTF (40) using its wrapper in

RELION-3 (version 3.07) (41-44) and then the extracted particle stacks were subjected to multiple rounds of 2D classification using RELION-3 or CryoSparc2 (45) for conformational analysis.

Cryo-electron microscopy sample preparation and imaging protocol

Freshly purified CST or CST-DNA complexes were directly used for cryo-EM grid preparation. We used either 1.2/1.3 μm 300 mesh copper C-flat (Protochips, USA) or gold Quantifoil (Quantifoil Micro Tools GmbH, Germany) grids. Prior to sample application, the cryo-EM grids were glow-discharged for 60 s at 45 mA using Emitech K100X glow discharger unit (Quorum Technologies, UK). For DNA-free CST samples (in buffer containing 50 mM HEPES-NaOH pH 7.5, 300 mM NaCl, 15 mM imidazole, 1 mM TCEP), we added a final concentration of 8 mM CHAPSO to the protein sample (10 mg/mL) for air-water interface protection (46) and immediately applied 4.0 μL of the sample to the cryo-EM grid before plunge-freezing using a Leica EM GP2 automatic plunge freezer (Leica Microsystems, USA). A dataset (6,424 movies) of this DNA-free CST cryo-EM sample was collected on the FEI Talos Arctica 200kV transmission electron microscope at the Anschutz Medical Campus (Colorado, USA) using the Leginon software (47). The movies were collected with a pixel size of 1.11 $\text{\AA}/\text{pixel}$, a defocus range of -2 to -3.5 μm , and a total dose of 53.6 $\text{e}/\text{\AA}^2$ (50 frames) using a Gatan K3 direct electron detector in counting mode (Gatan, USA).

For CST-3xTEL complexes, we added 1.2-fold excess of 5'-TTAGGGTTAGGGTTAGGG-3' DNA oligo (Integrated DNA Technologies, USA) and incubated on ice for 2 h (in similar buffer as a no-DNA sample but with either 300 mM or 500 mM NaCl without CHAPSO added) before applying the sample to cryo-EM grids. We found that adding CHAPSO caused severe particle aggregation, so we removed it in later stages of this work. For the 300 mM NaCl cryo-EM grids (where populations of CST monomeric and decameric particles are ~50%-50%, hereafter termed CST-3xTEL oligomer-mixture dataset), multiple datasets cumulating to a total of 11,503 movies were collected on FEI TECNAI F20 200 kV transmission electron microscope (using a 626 Gatan Cryo-holder with side-port entry) at the University of Colorado Boulder EM core facility using the SerialEM software (39). The movies were collected with a pixel size of 0.6095 $\text{\AA}/\text{pixel}$, a defocus range of -1.5 to -3.5 μm , and a total dose of 55.0 $\text{e}/\text{\AA}^2$ (50 frames) using a Gatan K3 direct electron detector in super-resolution mode (Gatan, USA).

For the 500 mM NaCl cryo-EM grids (where 90% of particles population is decameric, hereafter termed CST-3xTEL decamer dataset), two datasets of 0° (20,826 movies) and 30° (7,227 movies) stage-tilt were collected on the FEI Titan Krios 300 kV transmission electron microscope at the Janelia Research Campus Cryo-EM core facility (Ashburn, VA, USA) using SerialEM (39). Stage-tilt was done to resolve preferred-orientation problems of vitrified particles (48). The two datasets were collected with a pixel size of 0.539 $\text{\AA}/\text{pixel}$, a defocus range of -1 to -2.5 μm , and a total dose of 60.0 $\text{e}/\text{\AA}^2$ (60 frames) using a Gatan K3 direct electron detector in super-resolution CDS mode (Gatan, USA). A 3 x 3 beam tilt strategy with beam-tilt correction was implemented for both datasets.

Cryo-electron microscopy data processing

For the DNA-free CST dataset, movie frames (6,424 movies) were motion corrected with MotionCor2 (49) (9x9 patches and 3 frames grouping) before importing the aligned micrographs

into CryoSparc2 (45) for further processing. The micrograph CTF parameters were calculated using the CTFFIND4 (50) wrapper in CryoSparc2 pipeline. Images with poor CTF parameters were discarded and a curated stack of 4,174 micrographs was first denoised with JANNI (51) and then used for automated particle picking. A total of 1,236,394 auto-picked particles were extracted from original micrographs before being subjected to two rounds of 2D classification, yielding a final stack of 215,575 particles. An initial model was generated from CryoSparc2 *ab initio* reconstruction program and used as reference for CryoSparc2 heterogeneous refinement (3D classification) with four classes. This resulted in a single 3D class (~ 46 % of population) which was subjected to two rounds of CryoSparc2 *ab initio* reconstruction (using two classes) for further separation of particles with well-defined 3D features. The final subset of particles (53,747 particles) was subjected to homogeneous 3D refinement in CryoSparc2 which resulted in a 6.3 Å global resolution EM map based on the gold standard FSC cutoff threshold of 0.143.

For the CST-3xTEL oligomer-mixture dataset, the 11,503 movies were motion corrected (micrographs binned 2x from super-resolution pixel size during motion correction is described as 1x binned hereafter) as described above but using the wrapper in RELION-3 (41, 42, 44). GCTF (40) was used for calculation of CTF parameters on the aligned micrographs before curation based on CTF quality, leaving us with 6,706 micrographs. To pick out CST monomers amongst the mixtures of CST oligomeric states, we used the Laplacian-of-Gaussian (LoG) auto-picking function of RELION-3 with a circular mask encasing a single CST monomer. This resulted in 1,680,361 particles which we binned by four during particle extraction before subjecting the particles stack to two rounds of 2D classifications to remove junk particles, eventually yielding a stack of 775,577 particles. To further clean the particles stack, we used a low pass filtered (15 Å) DNA-free CST model (see prior paragraph) as a reference for a ten classes 3D classification. We selected a single class of 206,355 particles resembling the original DNA-free CST model, before re-extracting the particles without binning (1.219 Å/pixel) and re-centering based on the 3D classification alignments. Despite a second round of 3D classification using four classes, the particles in the good 3D class did not enrich further (206,263 particles), so we performed 3D refinement which led to a 10 Å map (postprocessed). We then did a third round of 3D classification using four classes, continuing from the alignments from the prior 3D refinement and now with a smaller sampling angle plus local angular searches. This resulted in two distinct classes representing the “head” and “arm” conformations (see main text for more details) on which we individually performed 3D refinement, leading to 8.9 Å and 9.2 Å global-resolution maps (values from postprocessing in RELION-3 software), respectively.

For the CST-3xTEL decamer samples, the 0° (20,826 movies) and 30° (7,227 movies) stage-tilt datasets were processed separately before combining at a later point. Both datasets were processed using the RELION-3 pipeline as described in the prior paragraph. Low pass filtered (20 Å) 2D templates of the CST decamer was first generated via a small scale (50 micrographs) LoG auto-picking and 2D classifications. The 2D templates were then used in the RELION-3 template-based auto-picking program to pick 4,437,008 and 2,546,827 particles from the curated aligned micrographs of 0° (15,952 micrographs) and 30° (6,967 micrographs) stage-tilt datasets, respectively. These particle stacks were extracted binned by four and then imported into Cryosparc2 for two rounds of 2D classification to clean up the auto-picked particles. This resulted in 821,497 and 194,846 particles from the 0° and 30° datasets, respectively. These particles stacks were then subjected to 3D classification using four classes in RELION-3 with an initial model generated by the CryoSparc2 *ab initio* reconstruction program. A single 3D class resolved with

high-resolution features was selected from each dataset (~27.5 – 31.1 % of population) and re-extracted without binning (1.078 Å/pixel) before performing 3D refinement with D5 symmetry imposed. This led to a 3.6 Å and 6.1 Å global resolution map (postprocessed) of the 0° and 30° datasets, respectively. The refined 3D alignments and models were used for CTF refinement (multiple times between 3D refinements), Bayesian particle polishing and beam-tilt refinement (41, 52) before performing a final 3D refinement, which led to 3.2 Å and 4.1 Å global-resolution map (postprocessed) of the 0° and 30° datasets, respectively. Both datasets were then combined (309,576 particles) and imported to CryoSparc2 for homologous 3D refinement using D5 symmetry, resulting in a 3.0 Å global resolution map (termed the consensus model). However, despite the high-resolution map reported from FSC, the map quality was still not sufficient for *de novo* building (53) due to monomer heterogeneity within the decameric complex.

To further resolve monomer heterogeneity (54) within a single decamer, we first used the consensus model refinement alignments to perform D5 symmetry expansion and then particle subtraction (55) using a decamer mask missing a single monomer (both steps done with RELION-3, soft masks made in Chimera (36)). This resulted in a subtracted and symmetry-expanded particle stack containing 3,095,760 particles (10-fold expansion) which was difficult to manage, so we subjected the particles stack to a 2.5-fold binning before performing masked 3D classification using eight classes and a low pass filtered (20 Å) reference monomer model. The 3D classification sampling angle was set at 1.8° with local angular searches enabled. This resulted in a single high-definition 3D class with 1,581,798 particles (~50% of input). We then referred the selected particles stack back to the non-subtracted and non-binned particles stack before performing masked (with a 9 pixels expansion to resolved decamer interfaces) 3D refinement with C1 symmetry, which led to a 3.1 Å global resolution map (postprocessed) and also an improved electron density map (fig. S5A). Local resolution was calculated using the RELION-3 local resolution program. To improve the local resolution of the CST “legs,” we designed a soft mask covering the legs and performed masked 3D classification with eight classes on the prior refined monomer model without any image alignments. This resulted in a single 3D class (~50%) where the legs region was well-defined. The selected particles from this 3D class were imported into CryoSparc2 for local refinement, resulting in a 3.0 Å global resolution map. Local resolution and sharpening were performed in Cryosparc2. Unless stated otherwise, all 3D classification and refinement steps were done with C1 symmetry. All RELION star files were manipulated using StarTool software (<https://github.com/cdienem/StarTool>) and particles files conversion from CryoSparc2 to RELION was done using UCSF PyEM software (<https://github.com/asarnow/pyem>).

Atomic model building, refinement and validation

Docking of CTC1 OB-E (Central OB-fold (25), PDB 5W2L), STN1n (N-terminal half, PDB 4JOI:A), STN1c (C-terminal half, PDB 4JQF) and TEN1 (PDB 4JOI:C) into the cryo-EM map were done using Chimera. The CTC1 atomic model was built using the final 3.0 Å global resolution cryo-EM map of the monomeric CST derived from the CST-3xTEL decamer dataset. Because of the multiple unstructured and unresolved linkers between the structured domains of CTC1, it was technically challenging to start atomic model building from the docked OB-E crystal structure. Hence, homology model for CTC1 was first generated using Phyre2 (56) (using Phyre2 *ab initio* modeling program that is based on primary sequence input) which we then used to dock into the cryo-EM map to nucleate *de novo* building. *De novo* building and sequence assignments

were manually curated and refined in Coot (57) using secondary structure prediction generated by PSIPRED (58) and bulky amino acid residues such as Arginine, Lysine, Histidine, Tyrosine, Phenylalanine and Tryptophan as guides. Because CTC1 N-terminal residues 1-140 were poorly resolved in the map, we were only able to build a ~ 45 residue poly-alanine main-chain model for this region.

The complete CST atomic model was refined against the cryo-EM map using the PHENIX real space refinement program (59) and then visually checked and again manually refined in Coot (57). As a final step, the model was subjected to PHENIX cryo-EM comprehensive validation program (MolProbity) (60) and EMringer (61) for model validation. Structural homology analysis was performed with DALI server (62) and based on the Z-score provided (against the full PDB database). Conservation analysis was done with ConSurf server (63). Surface area values were calculated using UCSF Chimera (36).

Electrophoretic mobility shift assay

Radioactive ^{32}P 5'-labeled singled-stranded oligonucleotides were used in the binding assays. The estimated specific activity was 200,000 c.p.m per pmol, and 500 c.p.m was used for each reaction (molar concentration of probe estimated to be < 0.1 nM). CST protein was either expressed and purified from insect cells (see above) or from HEK293T cells (see below), with equivalent results; CST containing R1175E CTC1 mutation was exclusively expressed in HEK293T cells. For binding, CST protein and DNA were mixed and incubated as a 10 μL reaction volume in binding buffer (20 mM HEPES-NaOH pH 8.0, 150 mM NaCl, 2 mM MgCl_2 , 0.2 mM EGTA, 0.1 % NP-40, 10 % glycerol, 1 mM TCEP) for 2 h on ice. The samples were then loaded into a pre-chilled 1x TBE 0.7 % agarose gel and electrophoresis proceeded at 7 V/cm for 1.5 h in a cold room (4 $^{\circ}\text{C}$). The gels were then vacuum dried at 80 $^{\circ}\text{C}$ until completely dried (~ 1.5 h) before exposing to a phosphorimager screen overnight. The screen was scanned with a Typhoon Trio scanner (GE Lifesciences, USA). Binding analysis was done with ImageQuant (Amersham, GE Life Sciences, USA) and the curve fitting performed ($\text{Fraction bound} = ([L]^n / ([L]^n + K_d^n))$) with KaleidaGraph (Synergy Software, USA). L is protein concentration, n is Hill coefficient and K_d is binding constant. Because replicates were typically done with independent protein preparations, which differed slightly in terms of percent active protein, the relative $K_{d,apparent}$ for each oligonucleotide was normalized to the $K_{d,apparent}$ of (TTAGGG)₃ determined on the same day with the same protein preparation.

Expression and purification of CST in human cells and testing oligomerization in vivo

HEK293T cells (ATCC, USA) were used for mammalian cell culture work. The cells were grown as adhered cells in DMEM medium supplemented with 2 mM L-glutamine, 1% penicillin/streptomycin, and 10% fetal bovine serum. 3xFLAG-CTC1, MYC-STN1 and HA-TEN1 mammalian expression plasmids were made for co-expression in HEK293T cells. Mutant constructs were made from these wild-type plasmids via standard mutagenesis and confirmed by Sanger sequencing. The three plasmids were stoichiometrically transfected into 70 - 80 % confluent one 10 cm plate or T175 flask of HEK293T cells using lipofectamine 2000 (Thermo Fisher Scientific, USA). After 24 h, the transfected cells were expanded to three times the culture volume and further incubated another 24 h before harvesting. The cells were then lysed using

CHAPS lysis buffer (10 mM Tris-HCl pH 7.5, 1 mM MgCl₂, 1 mM EGTA, 0.5% CHAPS, 10% glycerol, 5 mM β-mercaptoethanol, 1 mM PMSF) for 45 min at 4 °C while in a rotator. The cell lysate was clarified by centrifugation at 13,000 x g at 4 °C for 30 min. Pre-equilibrated (CHAPS lysis buffer) anti-FLAG M2 affinity resin was added to the clarified lysate and rotated for at least 4 h to overnight at 4 °C. The resin was washed three times with wash buffer (20 mM HEPES-NaOH pH 8.0, 150 mM NaCl, 2 mM MgCl₂, 0.2 mM EGTA, 0.1% NP-40, 10 % glycerol, 1 mM TCEP) before elution with 0.25 mg/mL 3xFLAG peptide (APExBIO, USA). Where indicated, the eluent was further mixed with pre-equilibrated (wash buffer) Anti-HA agarose resin (Thermo Fisher Scientific, USA) for 4 h at 4 °C before washing three times with wash buffer and eluted with 1 mg/mL HA peptide (APExBIO, USA).

For STN-CTC1 interaction mutation studies, only FLAG purification was performed, while for DNA-binding mutation studies, tandem-affinity purification of FLAG/HA purification was performed. For CST subunit analysis, western blots were performed to quantify immunoprecipitations of interacting subunits. Antibodies used were FLAG M2-HRP (Sigma Aldrich, USA), MYC-HRP (Thermo Fisher Scientific, USA) and HA-HRP (Thermo Fisher Scientific, USA). The molar concentrations of Wild-type and DNA-binding CST mutants were quantified by comparing against a standard titration curve (made with recombinant CST complex from insect cells) using a STN1 antibody (Novus Biological, USA). For orthogonal epitope tag pull-down experiments, the protocol is similar as the single purification step described above, with the following additional primary and secondary antibodies used: V5-HRP (Abcam, USA), STN1 mouse primary antibody (Novus Biological, USA), HA mouse primary antibody (BioLegend, USA) and HRP mouse secondary antibody (Jackson ImmunoResearch Laboratories, USA).

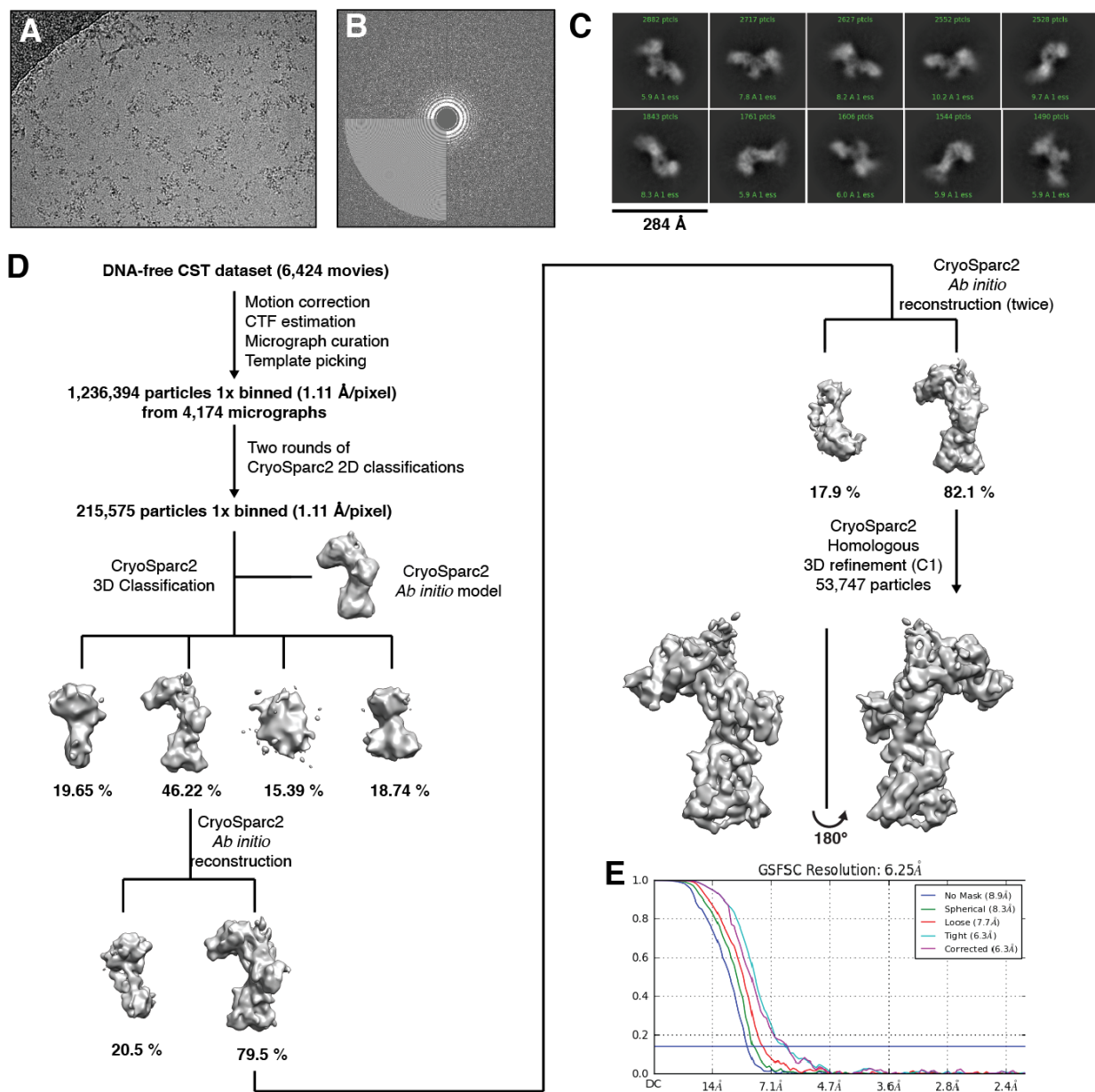


Fig. S1. Cryo-EM reconstruction of DNA-free monomeric CST complex. (A) A representative motion-corrected micrograph (denoised by JANNI (51)). (B) A representative calculated CTF image. (C) Top ten 2D classes selected after the final 2D classification step, showing various orientations of the DNA-free CST complex. (D) Cryo-EM processing pipeline of DNA-free CST. (E) CryoSparc2 (45) corrected Fourier shell correlation (FSC) reports a global resolution of 6.3 Å (purple curve).

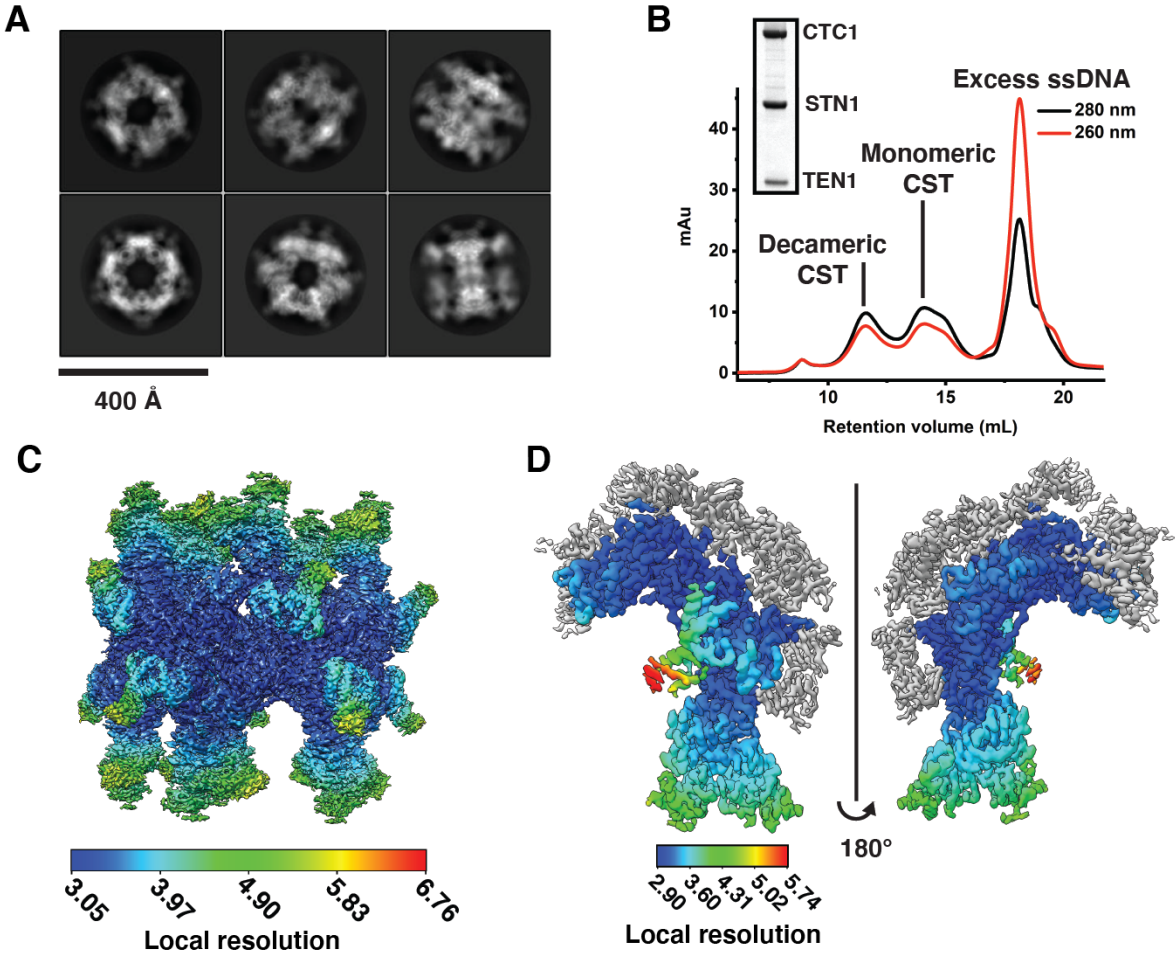


Fig. S2. Cryo-EM reconstruction of human CST decameric supercomplex. (A) Representative two-dimensional (2D) classes of CST-3xTEL particles. (B) Size-exclusion chromatography of human CST-ssDNA complexes resolves various oligomeric states. Inset, SDS-PAGE Coomassie-stained bands of the purified CST heterotrimeric complex – CTC1 (~135 kDa), STN1 (~42 kDa) and TEN1 (~14 kDa). (C) Cryo-EM density of CST-DNA decamer reconstructed from 3D refinement with D5 symmetry imposed. The model is colored based on local resolution (rainbow color scale-bar) (D) Cryo-EM density of CST-DNA monomer after symmetry expansion and three-dimensional (3D) classification. The grey density belongs to neighboring CST monomers in the decameric supercomplex. The monomeric model is colored based on local resolution (rainbow color scale-bar).

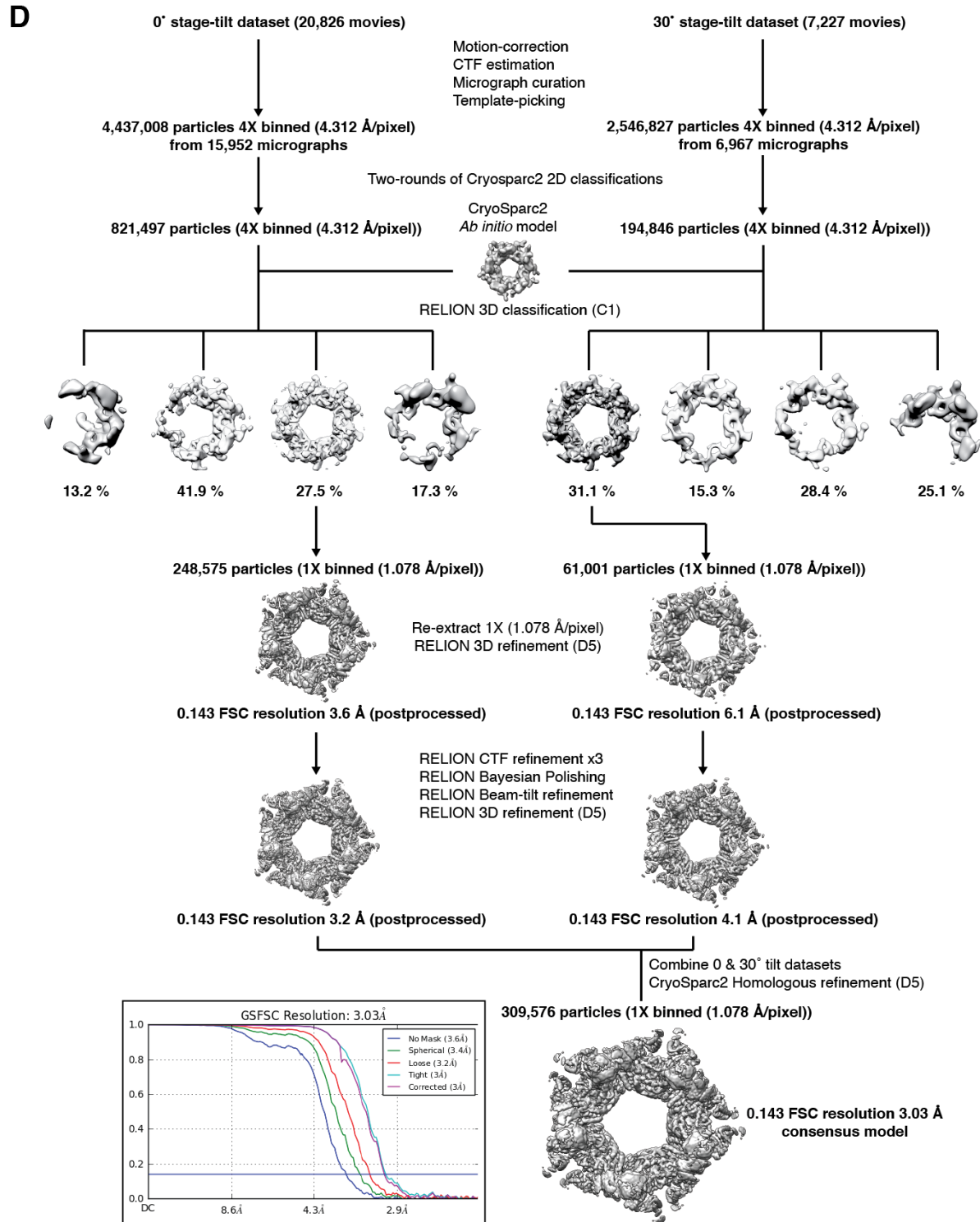
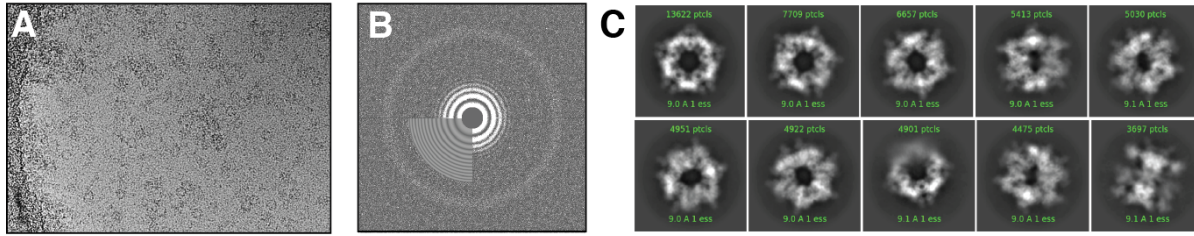


Fig. S3. Cryo-EM reconstruction of CST-3xTEL decamer complex. (A) A representative motion-corrected micrograph. (B) A representative calculated CTF image with water diffraction ring visible. (C) Top ten 2D classes selected after the final 2D classification step, showing various orientations of CST-3xTEL decamer complex. (D) Cryo-EM processing pipeline of stage-tilt datasets for CST-3xTEL decamer samples. Inset shows CryoSparc2 (45) corrected Fourier shell correlation (FSC) plot which reports a global resolution of 3.0 Å (purple curve).

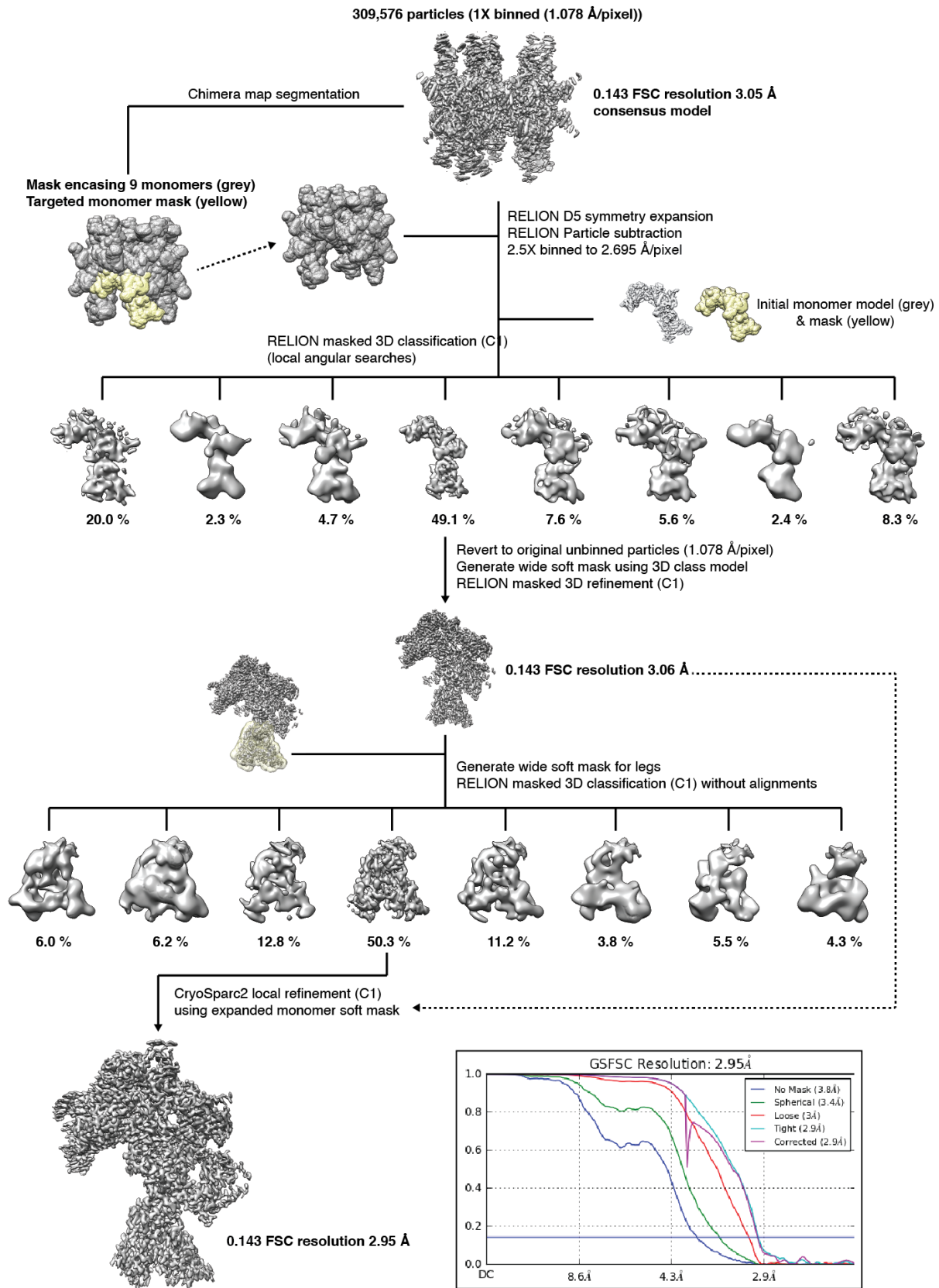


Figure S4. Conformational extraction of CST monomer from decamer complex for cryo-EM reconstruction. The DNA-free CST monomer model (fig. S1) was used as a guide to segment the decamer mask and remove a single monomer, resulting in a “10-1” soft mask. This mask was applied to the D5 symmetry expanded particle stack for particle subtraction, effectively removing nine CST monomers and leaving one monomer in a standardized position in the subtracted particle stack. 3D classification was used to identify a homogenous conformation for a CST monomer, which was carried forward for 3D refinement, leading to a 3.1 Å (rounded from 3.06 Å) map. A soft mask for the legs (see methods for details) was created to focus on isolating a population of particles with well-resolved legs region by 3D classification without alignments. The particles subset from a single 3D class showing well-defined “legs” were used for 3D refinement in CryoSparc2, leading to the final 3.0 Å (rounded from 2.95 Å) map used for *de novo* building.

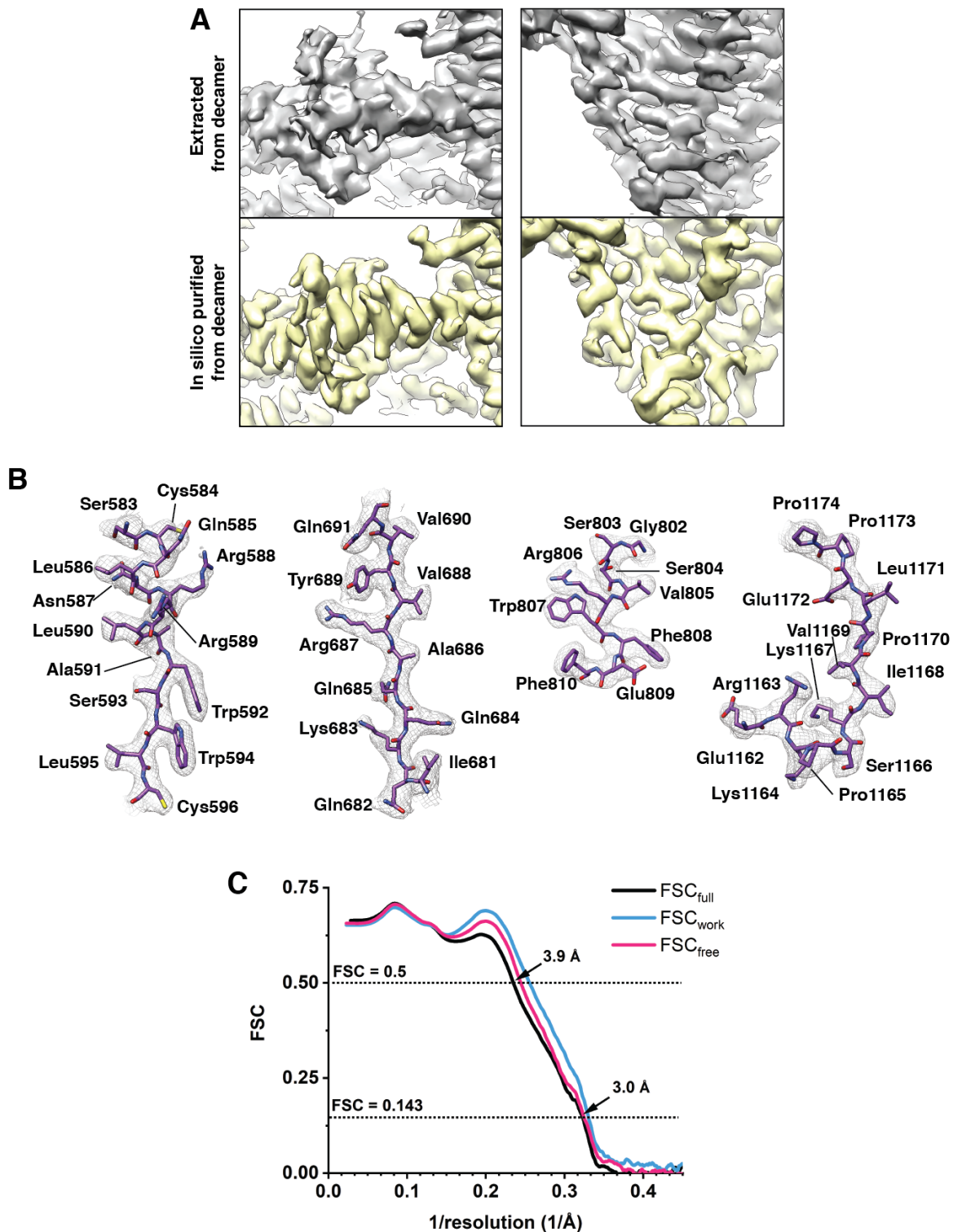


Figure S5. Quality differences between cryo-EM maps after *in silico* purification of CST monomer from decamer map, *de novo* model building and validation. (A) Comparison of the cryo-EM maps of CST monomer extracted directly from decamer consensus map (grey density) and *in silico* purified (yellow density, see fig. S4 and methods for monomer extraction details)

showing significant improvements in map interpretation. **(B)** Representative EM map density encasing the *de novo* built atomic models of CTC1. **(C)** Fourier-shell correlation plot of refined model to map (FSC_{full} , black curve) and half-maps validation of FSC_{work} and FSC_{free} (blue and pink curves, respectively).

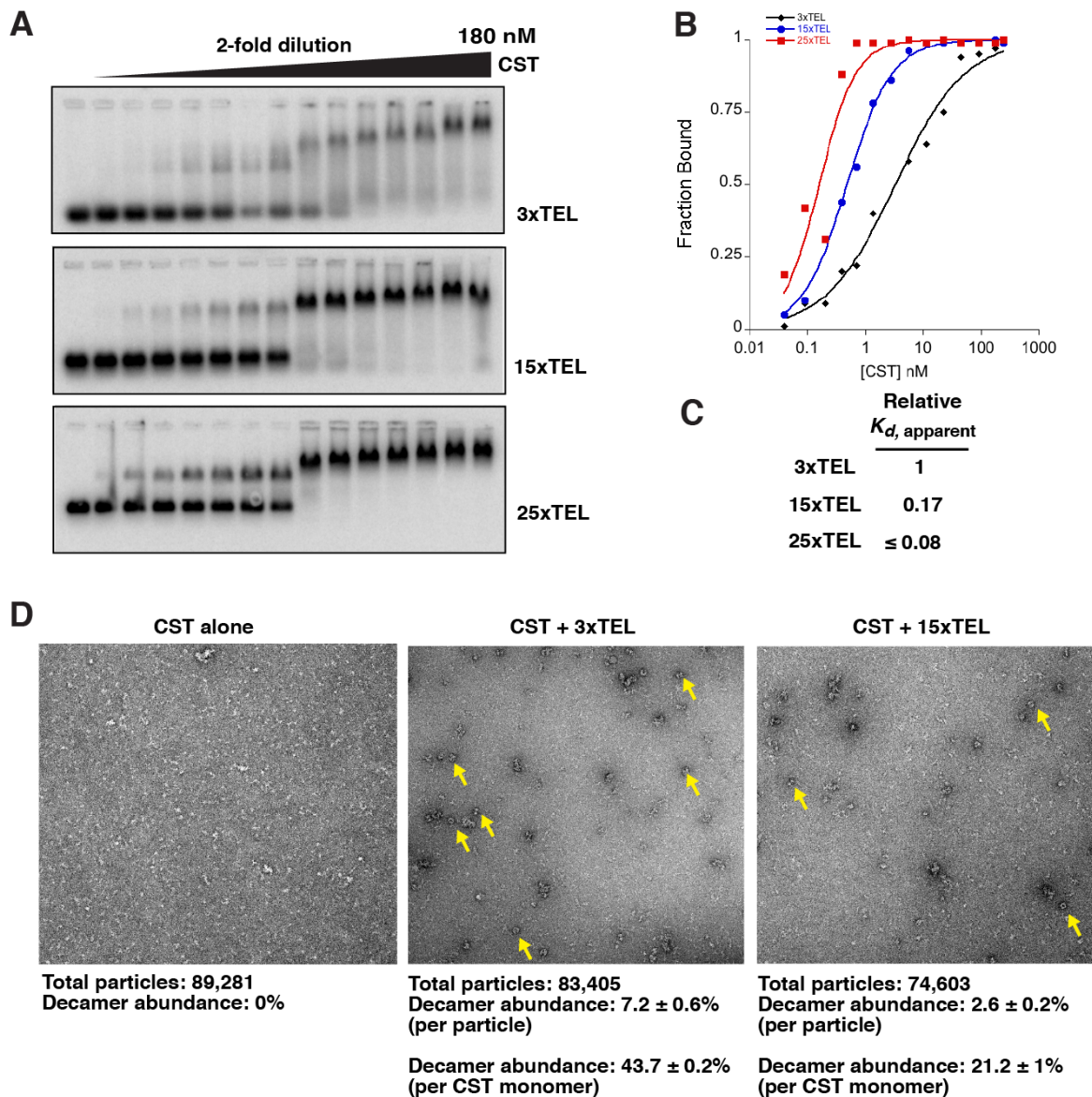


Figure S6. CST DNA-binding and structural analysis with longer telomeric single-stranded DNA molecules. (A) Gel-shift assay of purified CST complex (from HEK293T transfection) with 3x, 15x or 25xTEL ssDNA showed increasing CST binding affinity to longer telomeric ssDNA. (B) A representative plot of gel-shift assays with curve fitting (see method for curve fitting protocol) to derive binding constant ($K_{d, \text{apparent}}$). (C) The average relative $K_{d, \text{apparent}}$ values (normalized to 3xTEL values as unity) and their standard deviation across three independent gel-shift assays using two protein batches (see table S1 for absolute curve fitting values). The $K_{d, \text{apparent}}$ value of 25xTEL is a \leq approximation, as the concentration of the DNA in the binding assay is on the same order as the fitted K_d (see methods). (D) Negative-stain analysis of CST alone, with 3xTEL or 15xTEL ssDNA showed CST still forms decameric supercomplex (yellow arrows) with a longer telomeric ssDNA (15xTEL).

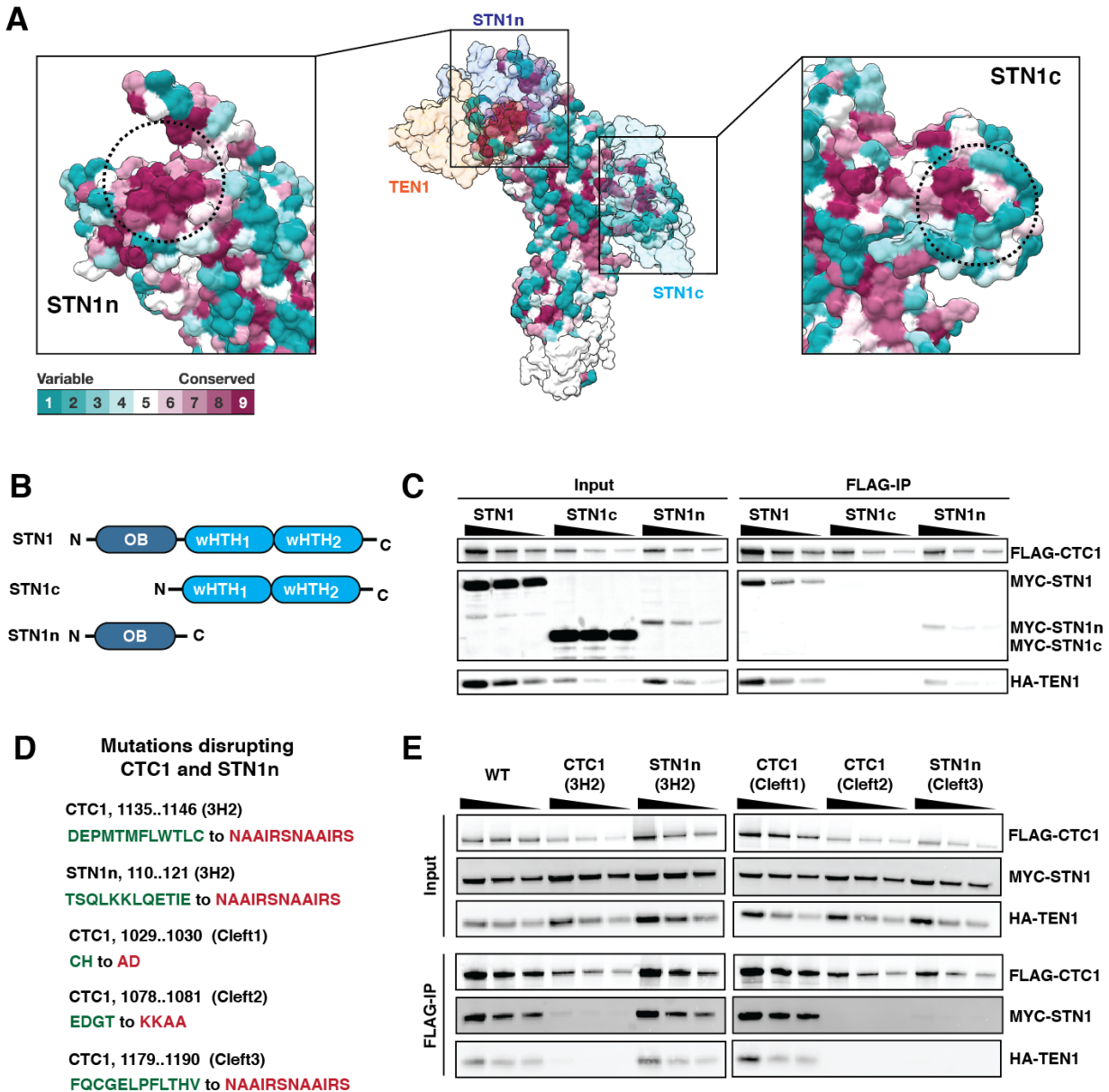


Figure S7. STN1 anchor site on CTC1. (A) ConSurf (63) analysis showing the conservation of CTC1 residues at the interaction sites of two STN1 subdomains – STN1n and STN1c. (B) Definitions of STN1n and STN1c. (C) FLAG-immunoprecipitation (FLAG-IP) of full-length STN1, STN1c and STN1n with 3xFLAG-CTC1 co-expressed in HEK293T cells. Based on the input samples, STN1n was less stably expressed than full-length STN1 and STN1c but was still able to bind CTC1 and TEN1, while STN1c did not stably associate. (D) Mutations designed to disrupt CTC1-STN1n interactions at CTC1 cleft region and newly identified CTC1-STN1n three-helix bundle (termed here, 3H2). STN1 (3H2) and CTC1 (3H2) mutants correspond to the annotated $\alpha 1$ and $\alpha 2$ of Fig. 2C. (E) Co-immunoprecipitation of co-expressed CST heterotrimeric complexes harboring the mutations showed CTC1 (3H2), CTC1 (Cleft1) and CTC1 (Cleft2)

mutations disrupted interaction between CTC1 and STN1, consistent with STN1n being the anchoring domain of STN1 to CTC1 (see panel C).

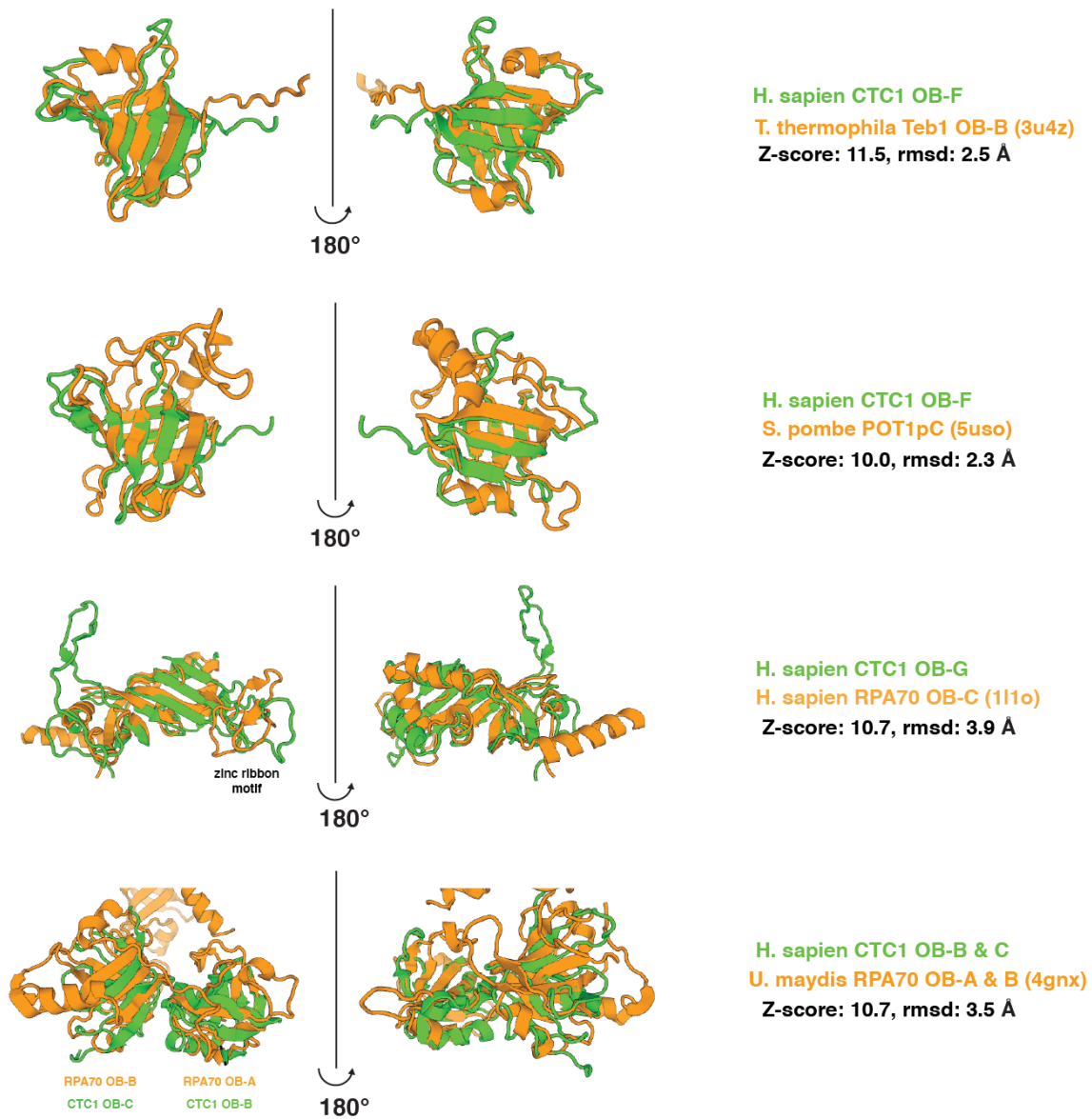
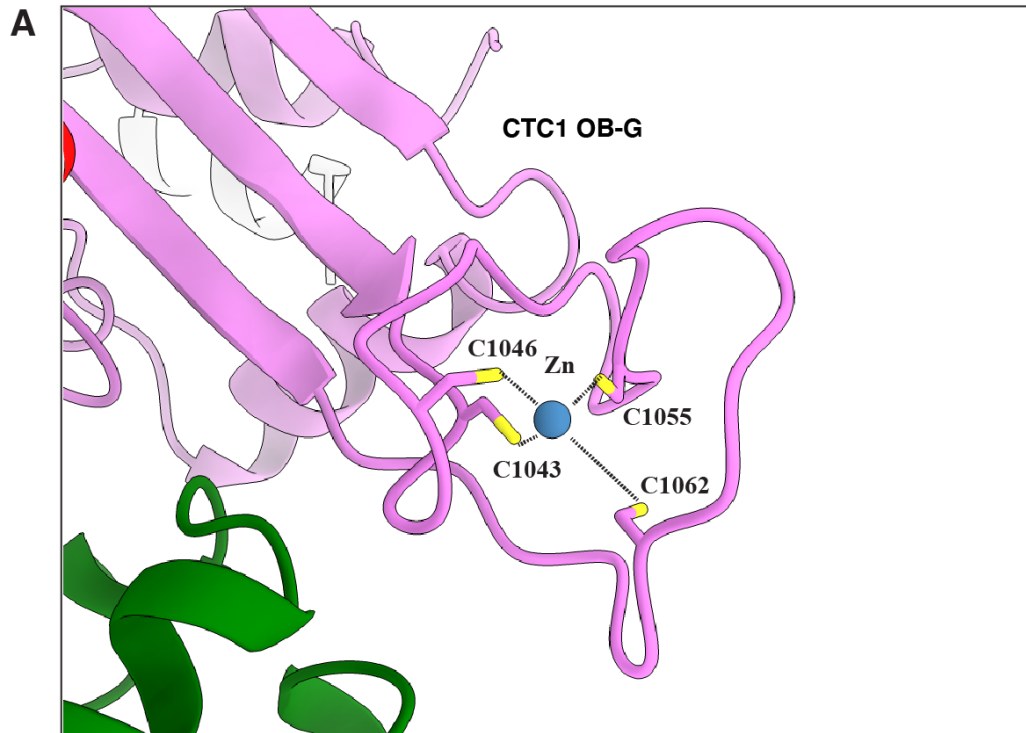


Figure S8. Structural homology search of CTC1 OB domains. (A) Top relevant structural homology hits of CTC1 OB-domains (B, C, F & G). The DALI webserver (62) was used to search for structural homology.



B

Variable	Conserved									C1043	C1046	C1055	C1062																																											
	1	2	3	4	5	6	7	8	9																																															
001 Input_pdb_ATGM_A	Q	Q	---	---	G	Q	S	---	P	F	Q	A	T	A	S	C	H	I	V	S	V	F	S	L	Q	L	F	W	V	C	A	Y	C	T	S	I	C	R	Q	G	K	C	D	R	L	G	S	T	C	T	Q	T	A			
002 <i>Sus scrofa</i> (Pig)	Q	Q	---	---	D	K	A	---	P	F	Q	A	T	A	S	C	H	I	V	S	V	F	S	L	Q	L	L	W	V	C	A	H	C	T	S	L	C	L	Q	G	K	C	D	R	Q	N	P	T	C	I	Q	T	P			
003 <i>Tupaia chinensis</i> (Chinese tree shrew)	Q	Q	---	---	S	Q	A	---	P	F	Q	A	T	A	S	C	H	I	V	S	V	F	S	L	A	L	L	W	V	C	H	C	T	S	I	C	P	Q	G	R	C	H	R	R	D	P	T	C	L	T	Q	T	S			
004 <i>Equus caballus</i> (Horse)	Q	Q	---	---	G	Q	A	---	P	F	Q	A	T	A	S	C	H	I	V	S	V	F	S	L	Q	L	F	W	V	C	A	H	C	T	S	L	C	P	Q	G	R	C	D	R	O	G	P	T	C	L	A	Q	T	S		
005 <i>Ochotona princeps</i> (South american pika)	Q	Q	---	---	G	Q	I	---	P	F	Q	A	T	A	S	C	H	I	V	S	V	F	S	L	Q	L	H	W	V	C	A	R	C	T	S	L	C	P	Q	G	R	C	D	R	O	S	P	A	C	S	T	Q	M	S		
006 <i>Erinaceus europaeus</i> (Euro.Hedgehog)	R	S	---	---	D	Q	T	---	P	F	Q	A	T	A	S	C	H	I	V	S	V	F	S	L	Q	L	R	W	V	C	S	H	C	T	S	L	C	V	Q	G	R	C	D	R	O	G	S	T	C	L	T	Q	T	S		
007 <i>Myotis lucifugus</i> (Little brown bat)	Q	Q	---	---	G	Q	A	---	P	F	Q	A	T	A	S	C	H	I	V	S	V	F	S	L	Q	L	R	W	V	C	A	H	C	T	S	V	S	I	Q	G	R	C	D	R	O	G	S	T	C	L	T	Q	T	S		
008 <i>Desmodus rotundus</i> (Vampire bat)	Q	Q	---	---	G	Q	A	---	P	F	Q	A	T	A	S	C	H	I	V	S	V	F	S	L	Q	L	L	W	V	C	A	H	C	T	S	L	F	I	Q	G	R	C	D	R	O	G	S	T	C	L	T	Q	T	S		
009 <i>Tarsius syrichta</i> (Phillpine tarsier)	Q	Q	---	---	S	R	A	---	P	F	Q	A	T	A	S	C	H	I	V	S	V	F	S	L	Q	L	S	W	V	C	A	H	C	T	S	I	C	S	Q	G	R	C	D	R	O	G	P	S	C	L	T	Q	T	S		
010 <i>Sorex araneus</i> (European shrew)	Q	Q	---	---	D	Q	A	---	P	F	Q	A	T	A	S	C	H	I	V	S	V	F	S	L	Q	L	L	W	V	C	A	H	C	G	C	L	C	L	Q	G	R	C	D	R	O	G	P	A	C	L	T	Q	T	S		
011 <i>Chrysochloris asiatica</i> (Cape golden mole)	H	G	---	---	H	Q	A	---	P	F	Q	A	T	A	S	C	H	I	V	S	V	F	S	L	Q	L	L	W	V	C	A	H	C	T	S	L	C	P	Q	G	K	C	S	H	O	G	P	A	C	L	T	Q	T	S		
012 <i>Cavia porcellus</i> (Guinea pig)	Q	Q	---	---	C	R	A	---	P	L	R	A	T	A	S	C	H	I	V	S	V	F	S	L	E	L	Q	W	V	C	A	H	C	S	S	V	C	L	Q	G	R	C	D	R	O	D	P	S	C	L	T	Q	T	S		
013 <i>Microtus ochrogaster</i> (Prairie vole)	Q	Q	---	---	G	Q	Q	V	P	F	Q	A	T	T	F	C	H	I	V	L	V	L	S	L	Q	I	L	W	V	C	A	H	C	T	S	I	S	P	Q	G	R	C	S	R	O	D	H	N	C	L	A	Q	T	A		
014 <i>Ictidomys tridecemlineatus</i> (Squirrel)	Q	S	---	---	S	C	G	---	P	F	Q	A	T	A	S	C	H	I	V	S	V	F	S	L	Q	L	R	W	V	C	A	H	C	T	S	V	C	P	Q	G	K	C	L	R	Q	G	P	T	C	L	T	Q	T	S		
015 <i>Cricetulus griseus</i> (Chinese hamster)	Q	Q	---	---	D	R	V	---	P	F	Q	A	T	T	S	C	H	I	V	L	V	L	S	L	Q	I	L	W	V	C	A	H	C	T	S	I	S	P	Q	G	R	C	S	R	O	D	H	N	C	L	A	Q	T	A		
016 <i>Miniopterus natalensis</i> (Natal bat)	Q	Q	---	---	G	Q	A	---	P	F	Q	A	T	A	S	C	H	I	V	S	V	F	S	L	Q	L	L	W	V	C	A	H	C	T	S	L	S	L	Q	G	R	C	D	R	O	G	S	I	C	L	T	P	T	F		
017 <i>Grammomys surdaster</i> (African thickert rat)	Q	Q	---	---	D	R	P	---	P	F	Q	A	T	I	S	C	H	I	V	V	L	S	L	Q	I	L	W	V	C	A	H	C	T	S	L	C	L	Q	G	K	C	S	R	R	D	P	S	C	L	T	Q	T	S			
018 <i>Loxodonta africana</i> (African elephant)	Q	Q	---	---	R	Q	A	---	P	F	Q	A	T	A	S	C	H	I	V	S	V	F	S	L	Q	L	L	W	V	C	A	H	C	T	S	L	C	L	Q	G	R	C	D	R	O	G	P	A	C	L	T	Q	T	S		
019 <i>Oryctolagus cuniculus</i> (Rabbit)	R	S	---	---	G	Q	T	---	P	F	Q	A	T	A	S	C	H	I	V	S	V	F	S	L	Q	L	R	W	V	C	A	H	C	T	S	F	C	P	Q	G	R	C	D	R	O	G	P	A	C	L	T	Q	T	S		
020 <i>Dipodomys ordii</i> (Ord's kangaroo rat)	R	S	---	---	G	P	A	---	P	F	Q	A	T	A	S	C	H	I	V	S	V	F	S	L	Q	L	L	W	V	C	A	H	C	T	S	V	C	L	Q	G	R	C	D	R	O	G	V	A	C	L	T	Q	A	S		
021 <i>Chinchilla lanigera</i> (Chinchilla villidera)	R	S	G	R	A	P	G	Q	A	---	P	F	Q	A	T	A	S	C	H	I	V	S	V	F	S	L	Q	L	L	W	V	C	A	H	C	S	G	V	C	P	Q	G	R	C	D	R	O	G	P	A	C	L	T	Q	T	S
022 <i>Suricata suricatta</i> (Meerkat)	Q	Q	---	---	R	R	A	---	P	F	Q	A	T	A	S	C	H	I	V	S	V	F	S	L	Q	L	L	W	V	C	A	H	C	T	S	L	C	P	Q	G	K	C	D	R	O	G	A	T	C	L	T	Q	T	S		
023 <i>Condylura cristata</i> (Star-nosed mole)	Q	Q	---	---	D	R	A	---	P	F	Q	A	T	A	F	C	H	I	V	T	V	F	S	L	Q	L	L	W	V	C	A	H	C	A	S	L	F	R	Q	G	R	C	D	R	O	G	P	A	C	L	T	Q	T	S		
024 <i>Galeopterus variegatus</i> (Malayan lemur)	Q	Q	---	---	G	R	A	---	P	F	Q	A	T	A	S	C	H	I	V	S	V	F	S	L	Q	L	L	W	V	C	A	H	C	T	S	I	C	P	Q	G	K	C	D	R	O	G	P	A	C	L	T	Q	T	S		
025 <i>Elephantulus edwardii</i> (elephant shrew)	Q	A	---	---	H	Q	A	---	P	F	Q	A	T	A	S	C	H	I	V	S	V	F	S	L	Q	L	C	W	V	C	H	C	T	S	L	A	P	Q	G	R	C	D	R	O	G	S	S	C	L	T	Q	T	S			
026 <i>Peromyscus maniculatus bairdii</i>	Q	Q	---	---	G	R	G	---	P	F	Q	A	T	A	S	C	H	I	V	S	V	F	S	L	Q	I	L	W	V	C	A	H	C	T	S	L	A	P	Q	G	R	C	S	R	O	D	H	N	C	L	A	Q	T	A		
027 <i>Sarcophilus harrisii</i> (Tasmanian devil)	R	S	---	---	S	P	G	---	P	T	H	A	S	A	S	C	H	V	S	V	L	S	V	Q	L	F	W	L	C	A	H	C	T	S	V	C	V	Q	G	Q	C	S	R	O	G	L	F	C	L	T	Q	A	S			

Figure S9. CTC1 zinc ribbon motif. (A) Modeled CTC1 zinc ribbon motif at OB-G domain, with four cysteines coordinating the zinc atom. (B) Cysteines (human protein numbering) involved in zinc coordination in the zinc ribbon motif are highly conserved. ConSurf webserver (63) was used for conservation analysis.

CTC1 OB domains

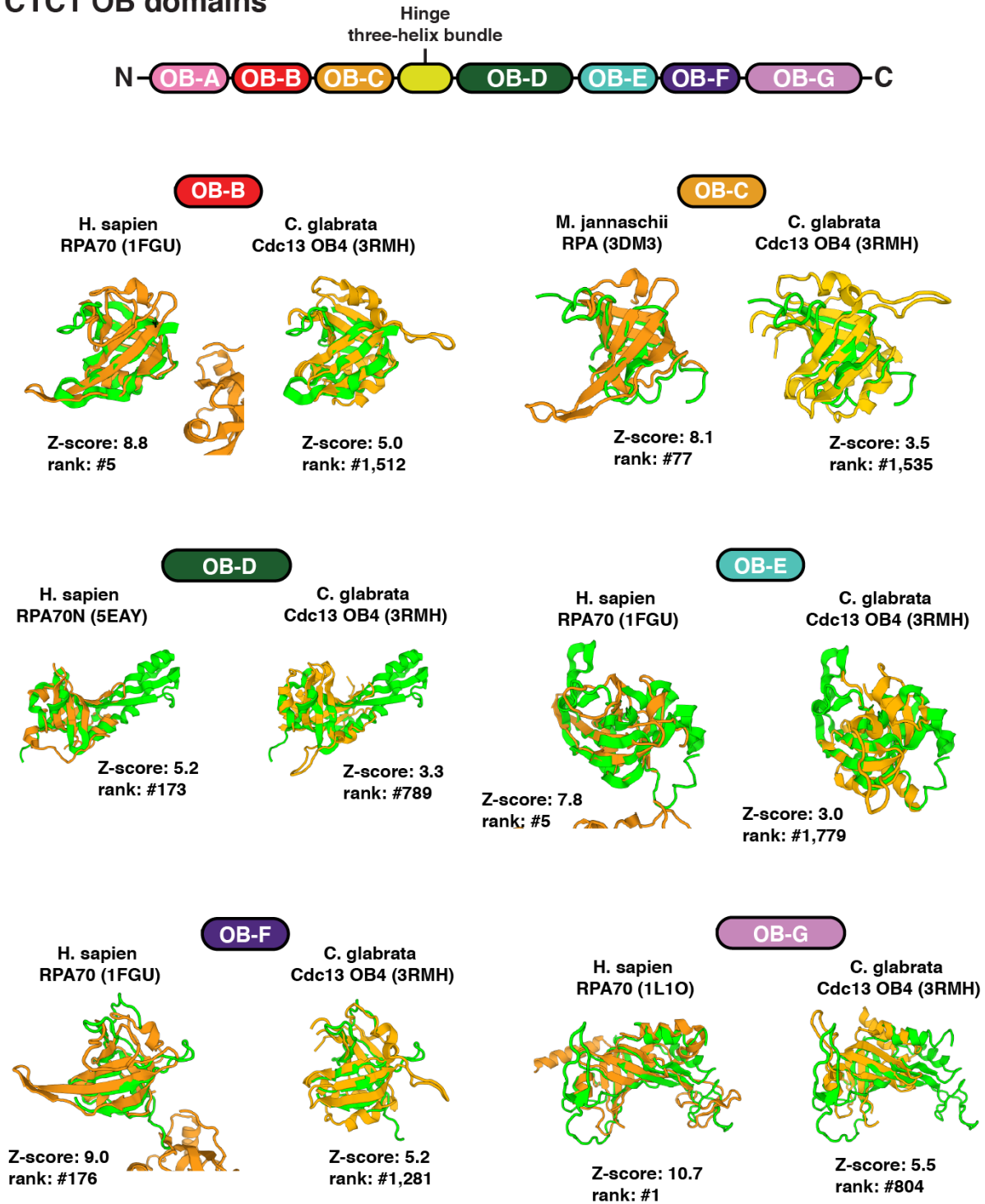


Figure S10. Structural homology comparison of human CTC1 against RPA70 or Cdc13 homologs. CTC1 individual OB-domains B, C, D, E, F & G were used to search for structural homologies using the DALI webserver (62). The top hits (based on Z-score) to RPA or to Cdc13 homologs were identified and compared for each CTC1 OB-domain. Their corresponding Z-score

and DALI ranking (searched against the entire PDB, PDB100) are shown below the overlapping models. CTC1 OB-domains are defined as CTC1₂₂₃₋₃₀₈ (OB-B), CTC1₃₅₀₋₄₄₉ (OB-C), CTC1₅₅₂₋₇₀₅ (OB-D), CTC1₇₂₅₋₈₆₄ (OB-E), CTC1₈₇₈₋₁₀₀₆ (OB-F) and CTC1₁₀₀₇₋₁₂₀₅ (OB-G).

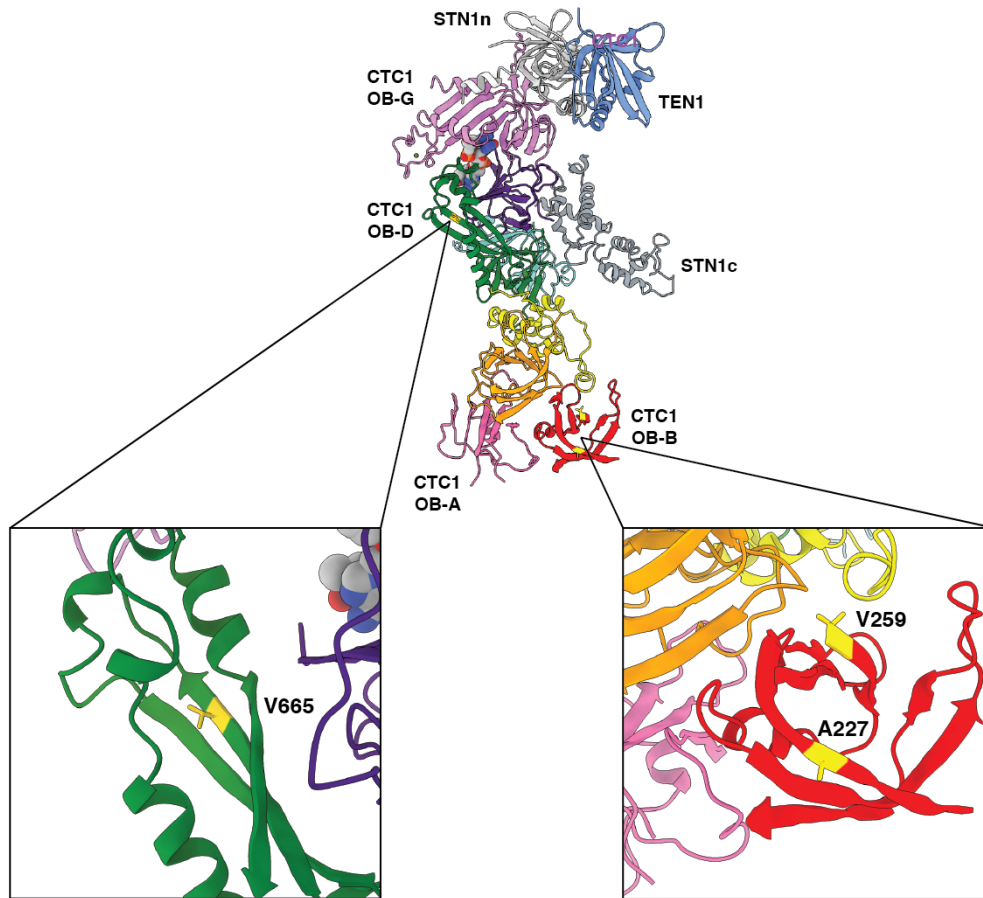


Figure S11. Structural mapping of CTC1 disease mutations that affect CST pol- α interaction. CTC1 residues (yellow) that are known to affect pol- α interaction with CST (A227, V259, V665) (15) are located in two separate sites at CTC1 OB-B and OB-D.

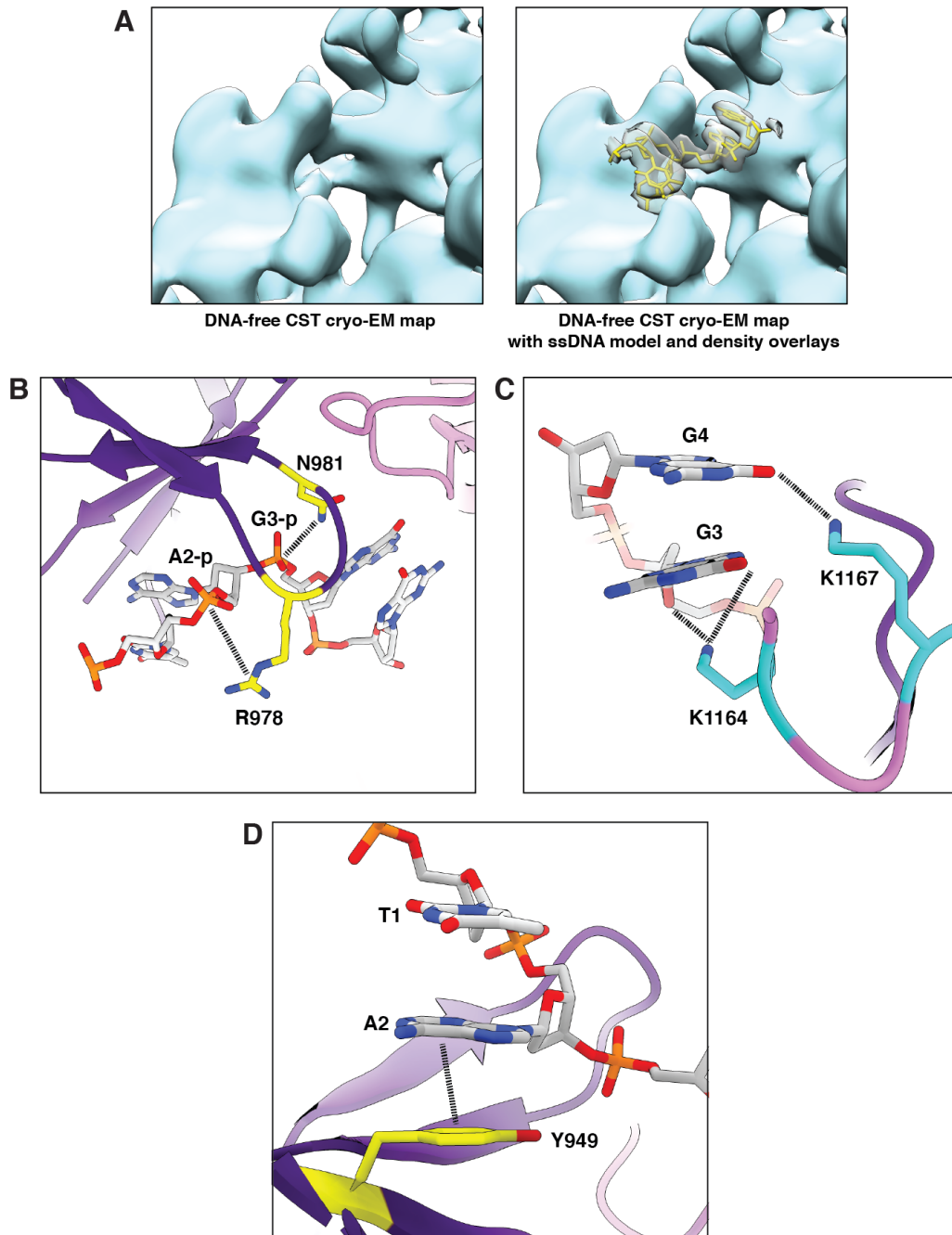


Figure S12. Single-stranded DNA EM density and its model interaction with CTC1 residues.

(A) The DNA-free CST EM map (turquoise, left panel) did not have the extra density of ssDNA (grey with yellow atomic model of ssDNA, right panel) that was found in the map of CST-3xTEL decamer. (B) CTC1 OB-F (yellow residues) interactions with phosphate groups of ssDNA. (C) CTC1 OB-G (cyan residues) interactions with DNA sugar and base. (D) CTC1 OB-F Y949 (yellow residue) π - π stacking with the A2 base which in turn is stacked on the T1 base.

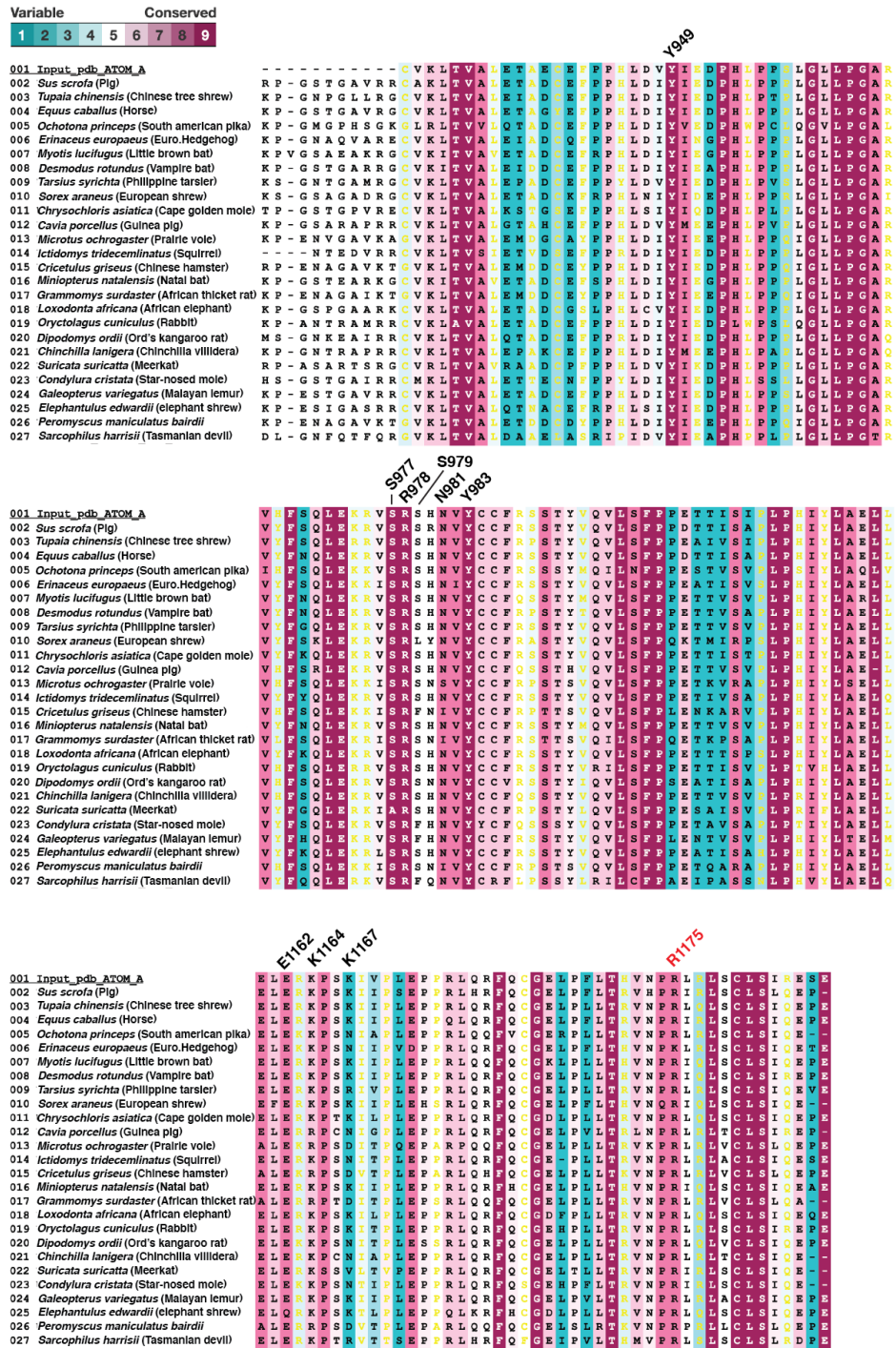


Figure S13. Residues conservation analysis of CTC1 DNA-binding mutants. ConSurf webserver (63) analysis of the conservation of identified DNA-binding residues of CTC1. Although CTC1 K1167 apparently has poor residue conservation, the variations were mostly limited to charged residues. CTC1 R1175 (red color) is an identified inter-molecular residue (see Fig. 4A) that interacts with ssDNA.

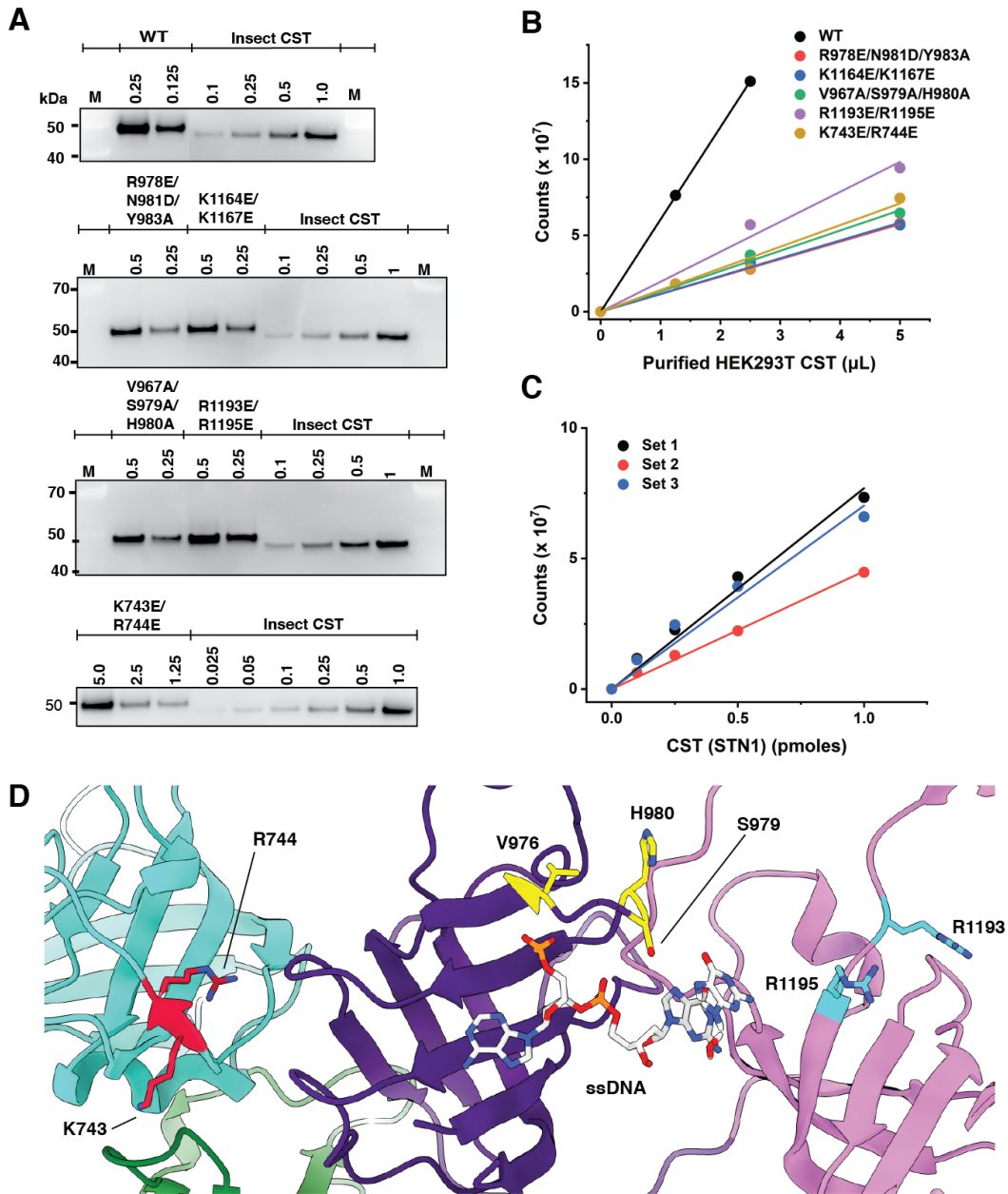


Figure S14. Quantification of mutant CST protein concentration and additional mutation residues mapping on atomic model. (A-C) Concentration quantification of HEK293T-derived CST complexes using recombinant insect cell CST as standard curve. STN1 western blot bands were used for comparison. **(B)** Dilution series of each CST complex (wild type (WT) or mutants) was performed to ensure western blot bands intensity scaled linearly. **(C)** Recombinant WT CST from insect cells was used to generate a standard curve for comparison (three independent sets shown). **(D)** Additional CTC1 amino acid residues (green or cyan) to those shown in Figure 3D that are chosen for DNA-binding mutagenesis. Yellow and cyan residues were DNA-binding defective upon mutagenesis. Red residues selected for DNA-binding control (see main text).

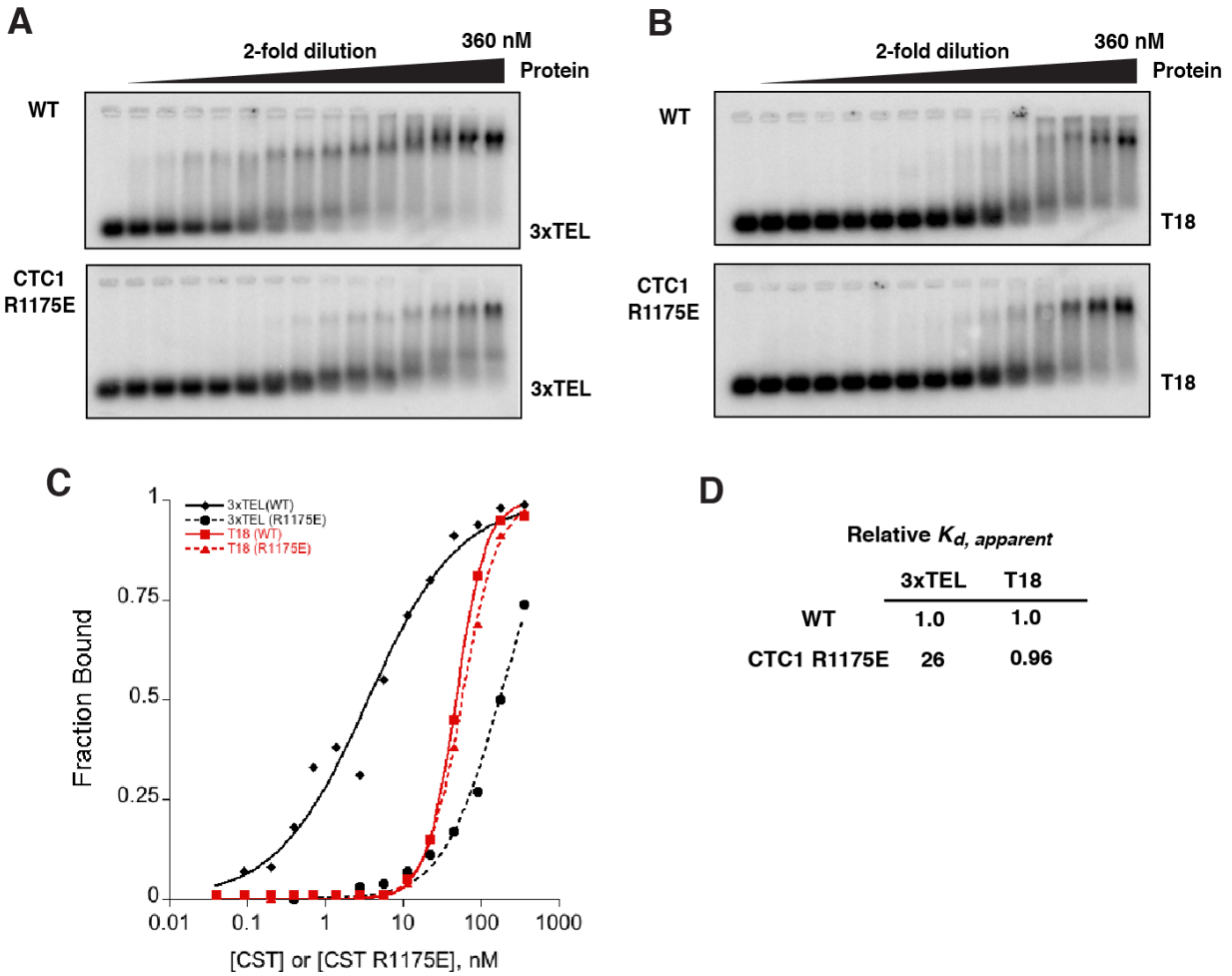


Figure S15. CTC1 R1175E binding analysis to specific and non-specific ssDNA. (A & B) Gel-shift assays of HEK293T-derived WT and CTC R1175E CST complexes with 3xTEL (specific ligand) and T18 (non-specific ligand, poly Ts with the same length 18nt as 3xTEL). Protein concentrations were similarly quantified using method described in fig. S14A-C. (C) A representative plot of gel-shift assays with curve fitting (see supplementary method for curve fitting protocol) to derive binding constant ($K_{d, \text{apparent}}$). (D) The average relative $K_{d, \text{apparent}}$ values (normalized to WT values as unity) and their standard deviation across three independent gel-shift assays using two protein batches.

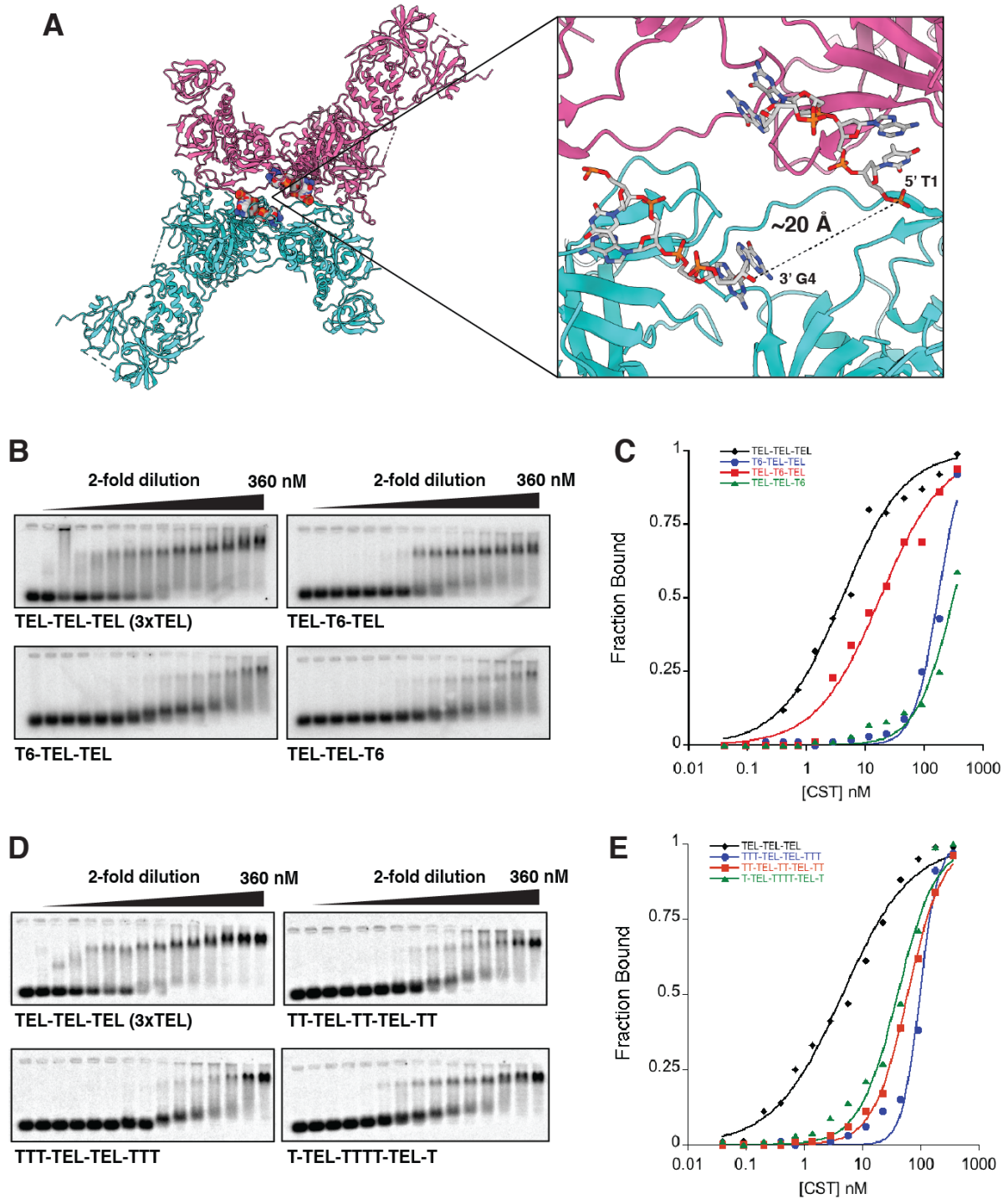


Figure S16. CST dimer stapling model structural and DNA-binding analysis. (A) Left panel shows a CST dihedral dimer (see main text for details). Right panel is the zoomed-in image of the two single-stranded DNA (ssDNA) molecules belonging to the dimer. Measured distance between the 5' T1 and 3' G4 of the opposite ssDNA is approximately 20 Å. A length of 20 Å will be equivalent to approximately 3 nucleotides (assuming a nucleotide spans 7 Å when fully extended). This is sufficient for a single (TTAGGG)₃ ssDNA molecule to engage both DNA anchor sites of

a CST dihedral dimer. **(B & C)** Gel-shift assays testing the effects of scrambling individual register of TTAGGG in the context of TEL-TEL-TEL (termed as 3xTEL in main text) to CST DNA-binding. **(D & E)** Gel-shift assays testing the effects of shortening of the linker between two TTAGGG sites to CST DNA-binding.

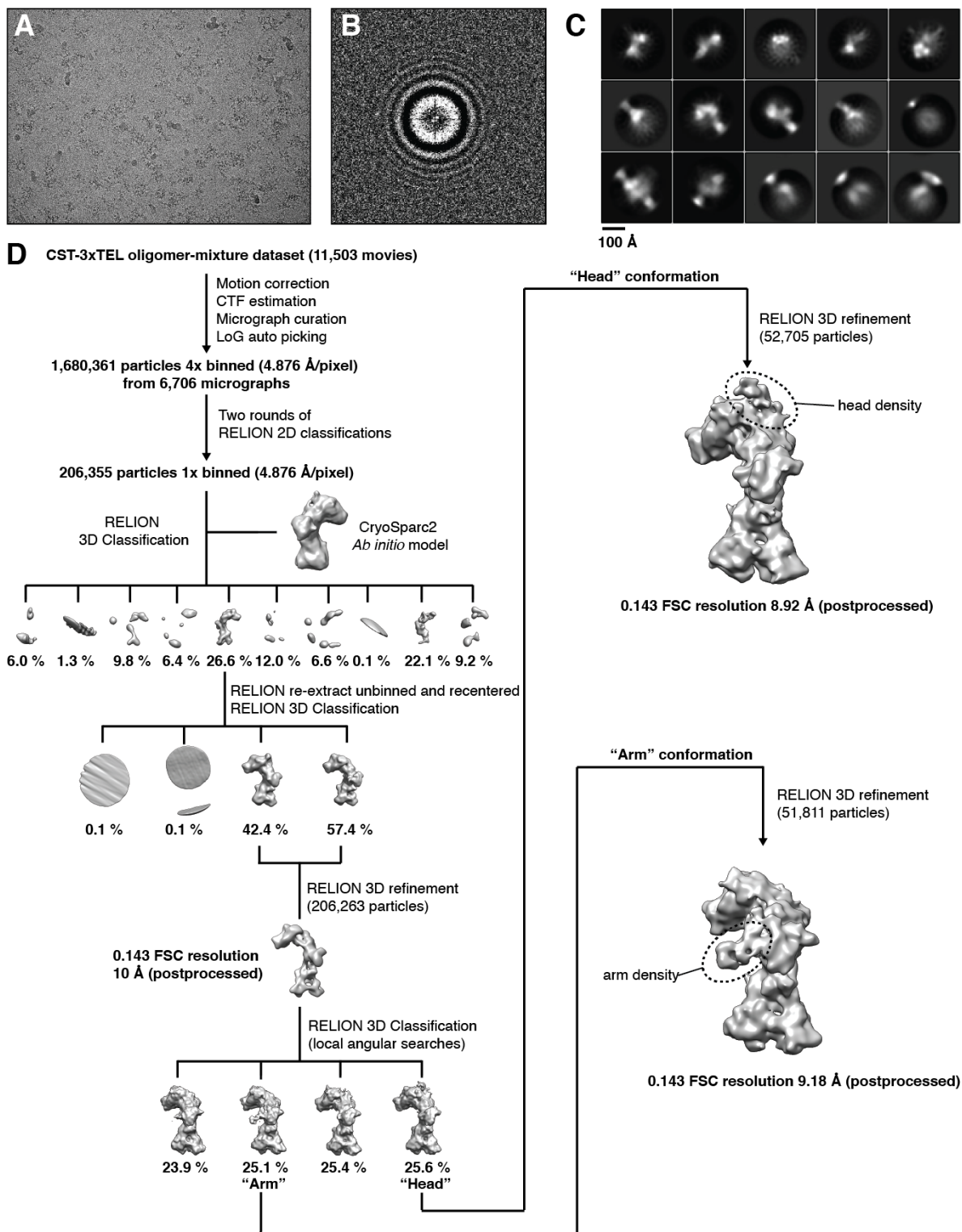


Fig. S17. Cryo-EM reconstruction of CST-3xTEL sample showing two distinct conformations. (A) A representative motion-corrected micrograph. (B) A representative

calculated CTF image. **(C)** Top fifteen 2D classes selected after the final 2D classification step. **(D)** Cryo-EM processing pipeline of DNA-free CST.

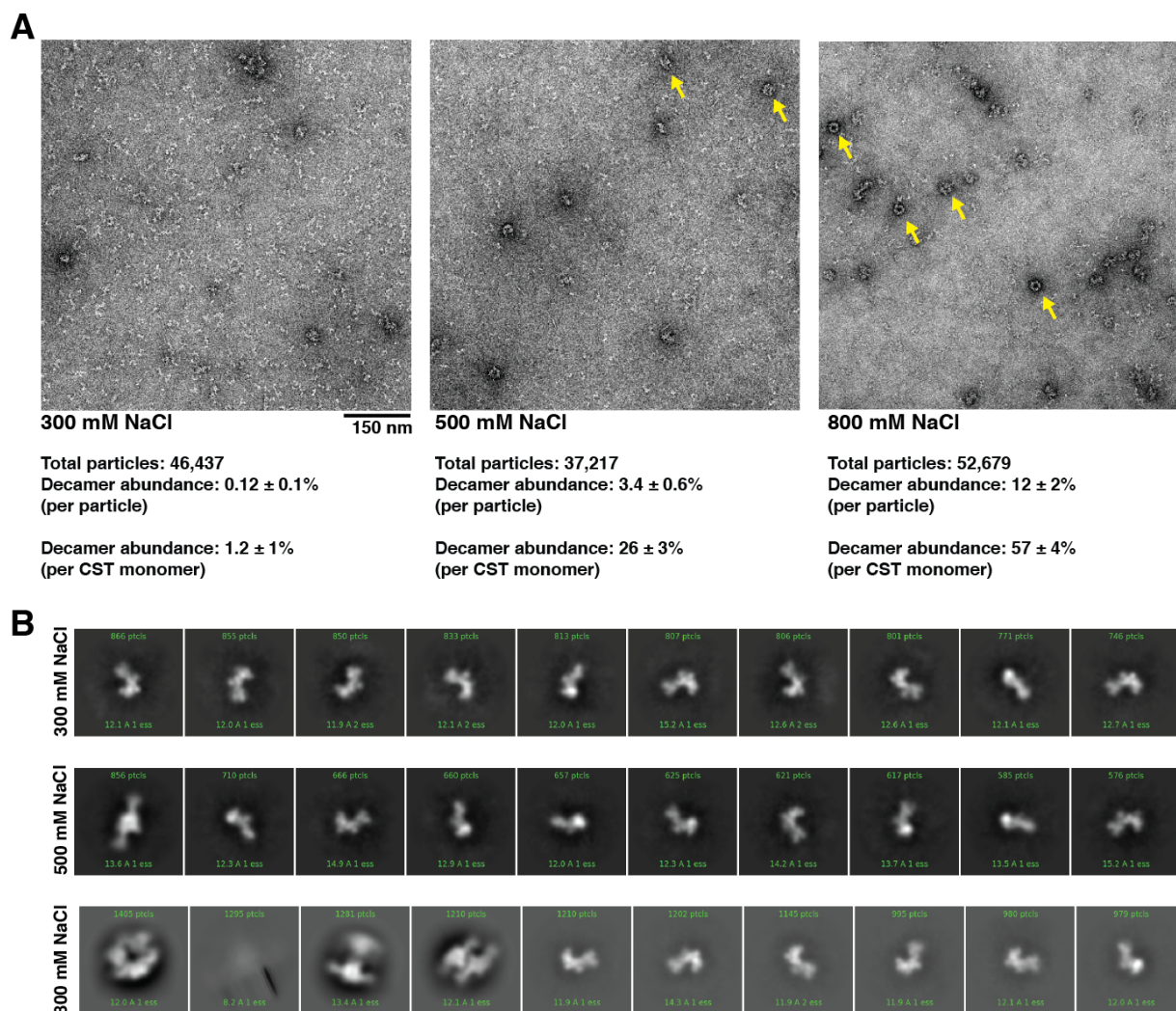


Figure S18. Negative-stain EM analysis of CST decamer formation salt-dependence. (A) Representative micrographs of CST incubated in buffers containing 300, 500 and 800 mM NaCl salt. Yellow arrows indicate CST decamer particles. **(B)** 2D classifications showing the top ten classes of particles (based on particles distribution). CST forms decameric particles with increasing NaCl concentration in buffer.

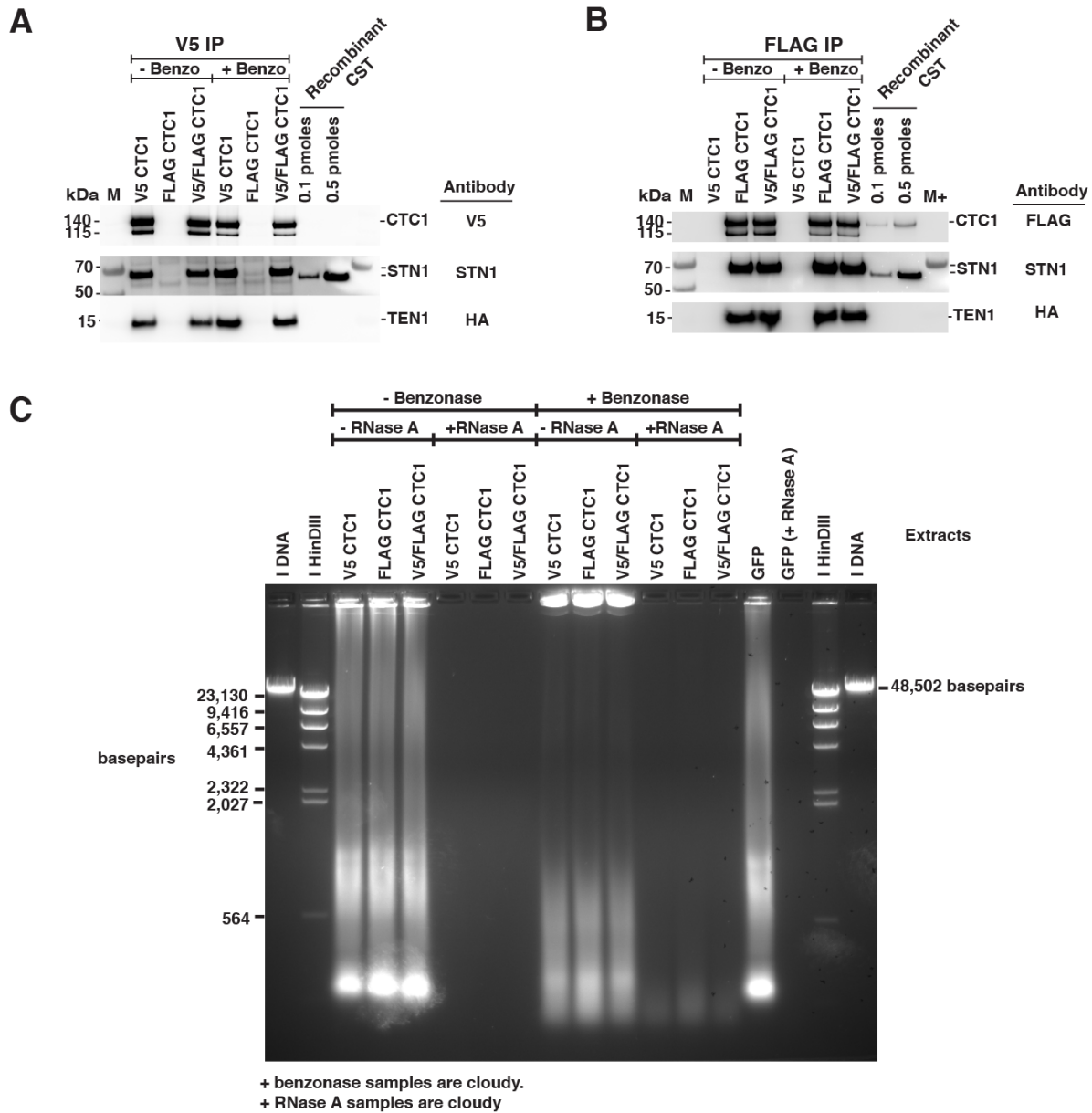


Figure S19. Controls for orthogonally tagged-CTC1 co-immunoprecipitation assay and benzonase treatment. (A & B) Control pull-downs for either V5- or FLAG-IP with co-transfected inputs. **(C)** Ethidium bromide stained agarose gel of cellular extracts treated with/without benzonase or RNase A suggests benzonase treatment degraded majority of nucleic acids in the inputs.

Sequence	Names	CST protein	$K_d, \text{apparent}$ 1st set	$K_d, \text{apparent}$ 2nd set	$K_d, \text{apparent}$ 3rd set	Average $K_d, \text{apparent}$	Standard Deviation
(TTAGGG) ₃	3xTEL	WT	3.4 (0.994)	5.9 (0.995)	9.0 (0.995)	6.1	2.8
(TTAGGG) ₁₅	15xTEL	WT	0.5 (0.998)	1.9 (0.993)	0.5 (0.973)	0.97	0.8
(TTAGGG) ₂₅	25xTEL	WT	0.2 (0.950)	0.9 (0.967)	0.2 (0.976)	0.43	0.4
(TTAGGG) ₃	3xTEL	WT	3.7 (0.986)	8.8 (0.996)	7.8 (0.996)	6.8	2.7
(TTAGGG) ₃	3xTEL	CTC1 _{R1175E}	170 (0.995)	190 (0.994)	77 (0.995)	150	63
T ₁₈	T18	WT	49 (0.999)	110 (0.999)	47 (0.999)	68	35
T ₁₈	T18	CTC1 _{R1175E}	58 (0.999)	90 (0.999)	41 (0.999)	63	25
T ₆ (TTAGGG) ₂	T6-TEL-TEL	WT	97 (0.996)	56 (0.994)	172 (0.987)	110	59
TTAGGG T ₆ TTAGGG	TEL-T6-TEL	WT	13 (0.993)	13 (0.992)	18 (0.989)	15	2.9
(TTAGGG) ₂ T ₆	TEL-TEL-T6	WT	156 (0.995)	64 (0.993)	50 (0.992)	89	56
TTTAGGGTTTTTAGGGT	T-TEL-TTTT-TEL-T	WT	130 (0.976)	67 (0.992)	41 (0.989)	78	44
TTTTAGGGTTTTAGGGTT	TT-TEL-TT-TEL-TT	WT	150 (0.996)	77 (0.994)	61 (0.999)	95	46
TTTTTAGGGTTAGGGTTT	TTT-TEL-TEL-TTT	WT	220 (0.997)	180 (0.992)	98 (0.992)	170	63

Table S1. Gel-shift DNA-binding assay experimental and curve fitting values. The absolute values of the fitted apparent binding constant ($K_d, \text{apparent}$) from three independent experiments are given in units of nanomolar (nM) with their corresponding R^2 values indicated in parentheses in *italics*. Except for the R^2 values (reported to three significant values), all values are reported to two significant figures.

CST complexes	DNA-free CST	CST-3xTEL oligomer-mixture	CST-3xTEL Decamer (0° tilt)	CST-3xTEL Decamer (30° tilt)	CST-3xTEL Decamer (0° + 30° tilt + D5 symmetry expanded)
Data collection and processing					
Magnification	36,000	29,000	81,000	81,000	81,000
Voltage (kV)	200	200	300	300	300
Electron exposure (e-/Å ²)	53.6	55.0	60.0	60.0	60.0
Defocus range (µm)	-2.0 to -3.5	-1.5 to -3.5	-1.0 to -2.5	-1.0 to -2.5	-1.0 to -2.5
Pixel size (Å)	1.11 (Count.)	0.6095 (Super.)	0.539 (Super.)	0.539 (Super.)	0.539 (Super.)
Symmetry imposed	C1	C1	D5	D5	C1
Initial particle images (no.)	1,236,394	1,680,361	4,437,008	2,546,827	3,095,760
Final particle images (no.)	53,747	52,705, 51,811	248,575	61,001	833,627
Map resolution (Å)	6.25	8.92, 9.18	3.2	4.1	2.95
FSC threshold	0.143	0.143	0.143	0.143	0.143
Refinement					
Initial model used (PDB code)					5W2L, 4JOI, 4JQF
Model resolution (Å)					3.30
FSC threshold					0.5
Map sharpening B factor (Å ²)					-80
Model composition					
Non-hydrogen atoms					11,054
Protein residues					1397
Ligands (DNA)					4
B factors (Å ²)					
Protein					120.23
Ligand (DNA)					131.46
R.m.s. deviations					
Bond lengths (Å)					0.007
Bond angles (°)					1.037
Validation					
MolProbity score					1.66
Clashscore					2.72
Poor rotamers (%)					0.00
Ramachandran plot					
Favored (%)					87.83
Allowed (%)					12.02
Disallowed (%)					0.15
EMRinger					3.49

Table S2. Cryo-EM data collection, refinement and validation statistics.

Sequence	CC ₁	CC ₂	CC ₃	CC ₄	CC _{overall}
TAGG	0.67	0.74	0.77	0.75	0.71
TTAG	0.66	0.73	0.77	0.65	0.70
GTTA	0.62	0.73	0.67	0.73	0.66
GGTT	0.61	0.68	0.65	0.65	0.63
GGGT	0.61	0.68	0.75	0.69	0.67
AGGG	0.62	0.68	0.76	0.75	0.68

Table S3. Cross-correlation analysis of the 4 nucleotides model building with cyclic permutation of telomeric DNA sequence. CC_n refers to the cross-correlation value of nucleotide to map at the position of nucleotide built from the 5' end. CC_{overall} is the computed overall cross-correlation value after model refinement. The table ranks the modeled sequence based on their CC_{overall} values. Model refinement and validation (where the CC values were derived) were done using Phenix software (59).

References and Notes

1. Y. V. Surovtseva, D. Churikov, K. A. Boltz, X. Song, J. C. Lamb, R. Warrington, K. Leehy, M. Heacock, C. M. Price, D. E. Shippen, Conserved telomere maintenance component 1 interacts with STN1 and maintains chromosome ends in higher eukaryotes. *Mol. Cell* **36**, 207–218 (2009). [doi:10.1016/j.molcel.2009.09.017](https://doi.org/10.1016/j.molcel.2009.09.017) [Medline](#)
2. Y. Miyake, M. Nakamura, A. Nabetani, S. Shimamura, M. Tamura, S. Yonehara, M. Saito, F. Ishikawa, RPA-like mammalian Ctc1-Stn1-Ten1 complex binds to single-stranded DNA and protects telomeres independently of the Pot1 pathway. *Mol. Cell* **36**, 193–206 (2009). [doi:10.1016/j.molcel.2009.08.009](https://doi.org/10.1016/j.molcel.2009.08.009) [Medline](#)
3. F. Wang, J. A. Stewart, C. Kasbek, Y. Zhao, W. E. Wright, C. M. Price, Human CST has independent functions during telomere duplex replication and C-strand fill-in. *Cell Rep.* **2**, 1096–1103 (2012). [doi:10.1016/j.celrep.2012.10.007](https://doi.org/10.1016/j.celrep.2012.10.007) [Medline](#)
4. L. Y. Chen, S. Redon, J. Lingner, The human CST complex is a terminator of telomerase activity. *Nature* **488**, 540–544 (2012). [doi:10.1038/nature11269](https://doi.org/10.1038/nature11269) [Medline](#)
5. D. E. Casteel, S. Zhuang, Y. Zeng, F. W. Perrino, G. R. Boss, M. Goulian, R. B. Pilz, A DNA polymerase- α primase cofactor with homology to replication protein A-32 regulates DNA replication in mammalian cells. *J. Biol. Chem.* **284**, 5807–5818 (2009). [doi:10.1074/jbc.M807593200](https://doi.org/10.1074/jbc.M807593200) [Medline](#)
6. M. Zhang, B. Wang, T. Li, R. Liu, Y. Xiao, X. Geng, G. Li, Q. Liu, C. M. Price, Y. Liu, F. Wang, Mammalian CST averts replication failure by preventing G-quadruplex accumulation. *Nucleic Acids Res.* **47**, 5243–5259 (2019). [doi:10.1093/nar/gkz264](https://doi.org/10.1093/nar/gkz264) [Medline](#)
7. A. Bhattacharjee, Y. Wang, J. Diao, C. M. Price, Dynamic DNA binding, junction recognition and G4 melting activity underlie the telomeric and genome-wide roles of human CST. *Nucleic Acids Res.* **45**, 12311–12324 (2017). [doi:10.1093/nar/gkx878](https://doi.org/10.1093/nar/gkx878) [Medline](#)
8. M. Chastain, Q. Zhou, O. Shiva, M. Fadri-Moskwik, L. Whitmore, P. Jia, X. Dai, C. Huang, P. Ye, W. Chai, Human CST Facilitates Genome-wide RAD51 Recruitment to GC-Rich Repetitive Sequences in Response to Replication Stress. *Cell Rep.* **16**, 1300–1314 (2016). [doi:10.1016/j.celrep.2016.06.077](https://doi.org/10.1016/j.celrep.2016.06.077) [Medline](#)
9. J. A. Stewart, F. Wang, M. F. Chaiken, C. Kasbek, P. D. Chastain 2nd, W. E. Wright, C. M. Price, Human CST promotes telomere duplex replication and general replication restart after fork stalling. *EMBO J.* **31**, 3537–3549 (2012). [doi:10.1038/emboj.2012.215](https://doi.org/10.1038/emboj.2012.215) [Medline](#)
10. K. Kratz, T. de Lange, Protection of telomeres 1 proteins POT1a and POT1b can repress ATR signaling by RPA exclusion, but binding to CST limits ATR repression by POT1b. *J. Biol. Chem.* **293**, 14384–14392 (2018). [doi:10.1074/jbc.RA118.004598](https://doi.org/10.1074/jbc.RA118.004598) [Medline](#)
11. Z. Mirman, F. Lottersberger, H. Takai, T. Kibe, Y. Gong, K. Takai, A. Bianchi, M. Zimmermann, D. Durocher, T. de Lange, 53BP1-RIF1-shieldin counteracts DSB resection through CST- and Pol α -dependent fill-in. *Nature* **560**, 112–116 (2018). [doi:10.1038/s41586-018-0324-7](https://doi.org/10.1038/s41586-018-0324-7) [Medline](#)
12. M. Greetham, E. Skordalakes, D. Lydall, B. A. Connolly, The Telomere Binding Protein Cdc13 and the Single-Stranded DNA Binding Protein RPA Protect Telomeric DNA from

- Resection by Exonucleases. *J. Mol. Biol.* **427**, 3023–3030 (2015).
[doi:10.1016/j.jmb.2015.08.002](https://doi.org/10.1016/j.jmb.2015.08.002) [Medline](#)
13. F. Wang, J. Stewart, C. M. Price, Human CST abundance determines recovery from diverse forms of DNA damage and replication stress. *Cell Cycle* **13**, 3488–3498 (2014).
[doi:10.4161/15384101.2014.964100](https://doi.org/10.4161/15384101.2014.964100) [Medline](#)
 14. J. A. Stewart, Y. Wang, S. M. Ackerson, P. L. Schuck, Emerging roles of CST in maintaining genome stability and human disease. *Front. Biosci.* **23**, 1564–1586 (2018).
[doi:10.2741/4661](https://doi.org/10.2741/4661) [Medline](#)
 15. L. Y. Chen, J. Majerská, J. Lingner, Molecular basis of telomere syndrome caused by CTC1 mutations. *Genes Dev.* **27**, 2099–2108 (2013). [doi:10.1101/gad.222893.113](https://doi.org/10.1101/gad.222893.113) [Medline](#)
 16. M. Armanios, An emerging role for the conserved telomere component 1 (CTC1) in human genetic disease. *Pediatr. Blood Cancer* **59**, 209–210 (2012). [doi:10.1002/psc.24200](https://doi.org/10.1002/psc.24200) [Medline](#)
 17. B. H. Anderson, P. R. Kasher, J. Mayer, M. Szykiewicz, E. M. Jenkinson, S. S. Bhaskar, J. E. Urquhart, S. B. Daly, J. E. Dickerson, J. O’Sullivan, E. O. Leibundgut, J. Muter, G. M. H. Abdel-Salem, R. Babul-Hirji, P. Baxter, A. Berger, L. Bonafé, J. E. Brunstom-Hernandez, J. A. Buckard, D. Chitayat, W. K. Chong, D. M. Cordelli, P. Ferreira, J. Fluss, E. H. Forrest, E. Franzoni, C. Garone, S. R. Hammans, G. Houge, I. Hughes, S. Jacquemont, P.-Y. Jeannet, R. J. Jefferson, R. Kumar, G. Kutschke, S. Lundberg, C. M. Lourenço, R. Mehta, S. Naidu, K. K. Nischal, L. Nunes, K. Öunap, M. Philippart, P. Prabhakar, S. R. Risen, R. Schiffmann, C. Soh, J. B. P. Stephenson, H. Stewart, J. Stone, J. L. Tolmie, M. S. van der Knaap, J. P. Vieira, C. N. Vilain, E. L. Wakeling, V. Wermenbol, A. Whitney, S. C. Lovell, S. Meyer, J. H. Livingston, G. M. Baerlocher, G. C. M. Black, G. I. Rice, Y. J. Crow, Mutations in CTC1, encoding conserved telomere maintenance component 1, cause Coats plus. *Nat. Genet.* **44**, 338–342 (2012).
[doi:10.1038/ng.1084](https://doi.org/10.1038/ng.1084) [Medline](#)
 18. M. Amir, T. Mohammad, V. Kumar, M. F. Alajmi, M. T. Rehman, A. Hussain, P. Alam, R. Dohare, A. Islam, F. Ahmad, M. I. Hassan, Structural Analysis and Conformational Dynamics of *STN1* Gene Mutations Involved in Coat Plus Syndrome. *Front. Mol. Biosci.* **6**, 41 (2019). [doi:10.3389/fmolb.2019.00041](https://doi.org/10.3389/fmolb.2019.00041) [Medline](#)
 19. P. Gu, S. Chang, Functional characterization of human CTC1 mutations reveals novel mechanisms responsible for the pathogenesis of the telomere disease Coats plus. *Aging Cell* **12**, 1100–1109 (2013). [doi:10.1111/accel.12139](https://doi.org/10.1111/accel.12139) [Medline](#)
 20. M. Lei, E. R. Podell, T. R. Cech, Structure of human POT1 bound to telomeric single-stranded DNA provides a model for chromosome end-protection. *Nat. Struct. Mol. Biol.* **11**, 1223–1229 (2004). [doi:10.1038/nsmb867](https://doi.org/10.1038/nsmb867) [Medline](#)
 21. D. Loayza, H. Parsons, J. Donigian, K. Hoke, T. de Lange, DNA binding features of human POT1: A nonamer 5'-TAGGGTTAG-3' minimal binding site, sequence specificity, and internal binding to multimeric sites. *J. Biol. Chem.* **279**, 13241–13248 (2004).
[doi:10.1074/jbc.M312309200](https://doi.org/10.1074/jbc.M312309200) [Medline](#)
 22. P. Baumann, T. R. Cech, Pot1, the putative telomere end-binding protein in fission yeast and humans. *Science* **292**, 1171–1175 (2001). [doi:10.1126/science.1060036](https://doi.org/10.1126/science.1060036) [Medline](#)

23. R. A. Hom, D. S. Wuttke, Human CST Prefers G-Rich but Not Necessarily Telomeric Sequences. *Biochemistry* **56**, 4210–4218 (2017). [doi:10.1021/acs.biochem.7b00584](https://doi.org/10.1021/acs.biochem.7b00584) [Medline](#)
24. C. Bryan, C. Rice, M. Harkisheimer, D. C. Schultz, E. Skordalakes, Structure of the human telomeric Stn1-Ten1 capping complex. *PLOS ONE* **8**, e66756 (2013). [doi:10.1371/journal.pone.0066756](https://doi.org/10.1371/journal.pone.0066756) [Medline](#)
25. P. K. Shastrula, C. T. Rice, Z. Wang, P. M. Lieberman, E. Skordalakes, Structural and functional analysis of an OB-fold in human Ctc1 implicated in telomere maintenance and bone marrow syndromes. *Nucleic Acids Res.* **46**, 972–984 (2018). [doi:10.1093/nar/gkx1213](https://doi.org/10.1093/nar/gkx1213) [Medline](#)
26. N. F. Lue, R. Zhou, L. Chico, N. Mao, O. Steinberg-Neifach, T. Ha, The telomere capping complex CST has an unusual stoichiometry, makes multipartite interaction with G-Tails, and unfolds higher-order G-tail structures. *PLOS Genet.* **9**, e1003145 (2013). [doi:10.1371/journal.pgen.1003145](https://doi.org/10.1371/journal.pgen.1003145) [Medline](#)
27. E. Bochkareva, S. Korolev, S. P. Lees-Miller, A. Bochkarev, Structure of the RPA trimerization core and its role in the multistep DNA-binding mechanism of RPA. *EMBO J.* **21**, 1855–1863 (2002). [doi:10.1093/emboj/21.7.1855](https://doi.org/10.1093/emboj/21.7.1855) [Medline](#)
28. J. Fan, N. P. Pavletich, Structure and conformational change of a replication protein A heterotrimer bound to ssDNA. *Genes Dev.* **26**, 2337–2347 (2012). [doi:10.1101/gad.194787.112](https://doi.org/10.1101/gad.194787.112) [Medline](#)
29. B. Wan, T. Tang, H. Upton, J. Shuai, Y. Zhou, S. Li, J. Chen, J. S. Brunzelle, Z. Zeng, K. Collins, J. Wu, M. Lei, The Tetrahymena telomerase p75-p45-p19 subcomplex is a unique CST complex. *Nat. Struct. Mol. Biol.* **22**, 1023–1026 (2015). [doi:10.1038/nsmb.3126](https://doi.org/10.1038/nsmb.3126) [Medline](#)
30. J. Jiang, H. Chan, D. D. Cash, E. J. Miracco, R. R. Ogorzalek Loo, H. E. Upton, D. Cascio, R. O'Brien Johnson, K. Collins, J. A. Loo, Z. H. Zhou, J. Feigon, Structure of Tetrahymena telomerase reveals previously unknown subunits, functions, and interactions. *Science* **350**, aab4070 (2015). [doi:10.1126/science.aab4070](https://doi.org/10.1126/science.aab4070) [Medline](#)
31. Z. Zeng, B. Min, J. Huang, K. Hong, Y. Yang, K. Collins, M. Lei, Structural basis for Tetrahymena telomerase processivity factor Teb1 binding to single-stranded telomeric-repeat DNA. *Proc. Natl. Acad. Sci. U.S.A.* **108**, 20357–20361 (2011). [doi:10.1073/pnas.1113624108](https://doi.org/10.1073/pnas.1113624108) [Medline](#)
32. D. L. Theobald, R. M. Mitton-Fry, D. S. Wuttke, Nucleic acid recognition by OB-fold proteins. *Annu. Rev. Biophys. Biomol. Struct.* **32**, 115–133 (2003). [doi:10.1146/annurev.biophys.32.110601.142506](https://doi.org/10.1146/annurev.biophys.32.110601.142506) [Medline](#)
33. C. Rice, E. Skordalakes, Structure and function of the telomeric CST complex. *Comput. Struct. Biotechnol. J.* **14**, 161–167 (2016). [doi:10.1016/j.csbj.2016.04.002](https://doi.org/10.1016/j.csbj.2016.04.002) [Medline](#)
34. R. Núñez-Ramírez, S. Klinge, L. Sauguet, R. Melero, M. A. Recuero-Checa, M. Kilkenny, R. L. Perera, B. García-Alvarez, R. J. Hall, E. Nogales, L. Pellegrini, O. Llorca, Flexible tethering of primase and DNA Pol α in the eukaryotic primosome. *Nucleic Acids Res.* **39**, 8187–8199 (2011). [doi:10.1093/nar/gkr534](https://doi.org/10.1093/nar/gkr534) [Medline](#)

35. L. Y. Chen, J. Lingner, CST for the grand finale of telomere replication. *Nucleus* **4**, 277–282 (2013). [doi:10.4161/nucl.25701](https://doi.org/10.4161/nucl.25701) [Medline](#)
36. E. F. Pettersen, T. D. Goddard, C. C. Huang, G. S. Couch, D. M. Greenblatt, E. C. Meng, T. E. Ferrin, UCSF Chimera—A visualization system for exploratory research and analysis. *J. Comput. Chem.* **25**, 1605–1612 (2004). [doi:10.1002/jcc.20084](https://doi.org/10.1002/jcc.20084) [Medline](#)
37. M. Pelosse, H. Crocker, B. Gorda, P. Lemaire, J. Rauch, I. Berger, MultiBac: From protein complex structures to synthetic viral nanosystems. *BMC Biol.* **15**, 99 (2017). [doi:10.1186/s12915-017-0447-6](https://doi.org/10.1186/s12915-017-0447-6) [Medline](#)
38. M. Rames, Y. Yu, G. Ren, Optimized negative staining: A high-throughput protocol for examining small and asymmetric protein structure by electron microscopy. *J. Vis. Exp.*, e51087 (2014). [doi:10.3791/51087](https://doi.org/10.3791/51087) [Medline](#)
39. D. N. Mastronarde, Automated electron microscope tomography using robust prediction of specimen movements. *J. Struct. Biol.* **152**, 36–51 (2005). [doi:10.1016/j.jsb.2005.07.007](https://doi.org/10.1016/j.jsb.2005.07.007) [Medline](#)
40. K. Zhang, Gctf: Real-time CTF determination and correction. *J. Struct. Biol.* **193**, 1–12 (2016). [doi:10.1016/j.jsb.2015.11.003](https://doi.org/10.1016/j.jsb.2015.11.003) [Medline](#)
41. J. Zivanov, T. Nakane, B. O. Forsberg, D. Kimanius, W. J. H. Hagen, E. Lindahl, S. H. W. Scheres, New tools for automated high-resolution cryo-EM structure determination in RELION-3. *eLife* **7**, e42166 (2018). [doi:10.7554/eLife.42166](https://doi.org/10.7554/eLife.42166) [Medline](#)
42. D. Kimanius, B. O. Forsberg, S. H. Scheres, E. Lindahl, Accelerated cryo-EM structure determination with parallelisation using GPUs in RELION-2. *eLife* **5**, e18722 (2016). [doi:10.7554/eLife.18722](https://doi.org/10.7554/eLife.18722) [Medline](#)
43. S. H. Scheres, Semi-automated selection of cryo-EM particles in RELION-1.3. *J. Struct. Biol.* **189**, 114–122 (2015). [doi:10.1016/j.jsb.2014.11.010](https://doi.org/10.1016/j.jsb.2014.11.010) [Medline](#)
44. S. H. Scheres, RELION: Implementation of a Bayesian approach to cryo-EM structure determination. *J. Struct. Biol.* **180**, 519–530 (2012). [doi:10.1016/j.jsb.2012.09.006](https://doi.org/10.1016/j.jsb.2012.09.006) [Medline](#)
45. A. Punjani, J. L. Rubinstein, D. J. Fleet, M. A. Brubaker, cryoSPARC: Algorithms for rapid unsupervised cryo-EM structure determination. *Nat. Methods* **14**, 290–296 (2017). [doi:10.1038/nmeth.4169](https://doi.org/10.1038/nmeth.4169) [Medline](#)
46. A. J. Noble, H. Wei, V. P. Dandey, Z. Zhang, Y. Z. Tan, C. S. Potter, B. Carragher, Reducing effects of particle adsorption to the air-water interface in cryo-EM. *Nat. Methods* **15**, 793–795 (2018). [doi:10.1038/s41592-018-0139-3](https://doi.org/10.1038/s41592-018-0139-3) [Medline](#)
47. B. Carragher, N. Kisseberth, D. Kriegman, R. A. Milligan, C. S. Potter, J. Pulokas, A. Reilein, Legion: An automated system for acquisition of images from vitreous ice specimens. *J. Struct. Biol.* **132**, 33–45 (2000). [doi:10.1006/jsbi.2000.4314](https://doi.org/10.1006/jsbi.2000.4314) [Medline](#)
48. Y. Z. Tan, P. R. Baldwin, J. H. Davis, J. R. Williamson, C. S. Potter, B. Carragher, D. Lyumkis, Addressing preferred specimen orientation in single-particle cryo-EM through tilting. *Nat. Methods* **14**, 793–796 (2017). [doi:10.1038/nmeth.4347](https://doi.org/10.1038/nmeth.4347) [Medline](#)

49. S. Q. Zheng, E. Palovcak, J.-P. Armache, K. A. Verba, Y. Cheng, D. A. Agard, MotionCor2: Anisotropic correction of beam-induced motion for improved cryo-electron microscopy. *Nat. Methods* **14**, 331–332 (2017). [doi:10.1038/nmeth.4193](https://doi.org/10.1038/nmeth.4193) [Medline](#)
50. A. Rohou, N. Grigorieff, CTFFIND4: Fast and accurate defocus estimation from electron micrographs. *J. Struct. Biol.* **192**, 216–221 (2015). [doi:10.1016/j.jsb.2015.08.008](https://doi.org/10.1016/j.jsb.2015.08.008) [Medline](#)
51. T. Wagner, MPI-Dortmund/sphire-janni: JANNI 0.0.5 (Version v0.0.5). Zenodo., (2019).
52. J. Zivanov, T. Nakane, S. H. W. Scheres, A Bayesian approach to beam-induced motion correction in cryo-EM single-particle analysis. *IUCrJ* **6**, 5–17 (2019). [doi:10.1107/S205225251801463X](https://doi.org/10.1107/S205225251801463X) [Medline](#)
53. S. Subramaniam, L. A. Earl, V. Falconieri, J. L. Milne, E. H. Egelman, Resolution advances in cryo-EM enable application to drug discovery. *Curr. Opin. Struct. Biol.* **41**, 194–202 (2016). [doi:10.1016/j.sbi.2016.07.009](https://doi.org/10.1016/j.sbi.2016.07.009) [Medline](#)
54. S. H. Roh, C. F. Hryc, H.-H. Jeong, X. Fei, J. Jakana, G. H. Lorimer, W. Chiu, Subunit conformational variation within individual GroEL oligomers resolved by Cryo-EM. *Proc. Natl. Acad. Sci. U.S.A.* **114**, 8259–8264 (2017). [doi:10.1073/pnas.1704725114](https://doi.org/10.1073/pnas.1704725114) [Medline](#)
55. X. C. Bai, E. Rajendra, G. Yang, Y. Shi, S. H. Scheres, Sampling the conformational space of the catalytic subunit of human γ -secretase. *eLife* **4**, 4 (2015). [Medline](#)
56. L. A. Kelley, S. Mezulis, C. M. Yates, M. N. Wass, M. J. Sternberg, The Phyre2 web portal for protein modeling, prediction and analysis. *Nat. Protoc.* **10**, 845–858 (2015). [doi:10.1038/nprot.2015.053](https://doi.org/10.1038/nprot.2015.053) [Medline](#)
57. P. Emsley, B. Lohkamp, W. G. Scott, K. Cowtan, Features and development of Coot. *Acta Crystallogr. D Biol. Crystallogr.* **66**, 486–501 (2010). [doi:10.1107/S0907444910007493](https://doi.org/10.1107/S0907444910007493) [Medline](#)
58. D. T. Jones, Protein secondary structure prediction based on position-specific scoring matrices. *J. Mol. Biol.* **292**, 195–202 (1999). [doi:10.1006/jmbi.1999.3091](https://doi.org/10.1006/jmbi.1999.3091) [Medline](#)
59. P. V. Afonine, B. K. Poon, R. J. Read, O. V. Sobolev, T. C. Terwilliger, A. Urzhumtsev, P. D. Adams, Real-space refinement in PHENIX for cryo-EM and crystallography. *Acta Crystallogr. D Struct. Biol.* **74**, 531–544 (2018). [doi:10.1107/S2059798318006551](https://doi.org/10.1107/S2059798318006551) [Medline](#)
60. C. J. Williams, J. J. Headd, N. W. Moriarty, M. G. Prisant, L. L. Videau, L. N. Deis, V. Verma, D. A. Keedy, B. J. Hintze, V. B. Chen, S. Jain, S. M. Lewis, W. B. Arendall 3rd, J. Snoeyink, P. D. Adams, S. C. Lovell, J. S. Richardson, D. C. Richardson, MolProbity: More and better reference data for improved all-atom structure validation. *Protein Sci.* **27**, 293–315 (2018). [doi:10.1002/pro.3330](https://doi.org/10.1002/pro.3330) [Medline](#)
61. B. A. Barad, N. Echols, R. Y.-R. Wang, Y. Cheng, F. DiMaio, P. D. Adams, J. S. Fraser, EMRinger: Side chain-directed model and map validation for 3D cryo-electron microscopy. *Nat. Methods* **12**, 943–946 (2015). [doi:10.1038/nmeth.3541](https://doi.org/10.1038/nmeth.3541) [Medline](#)
62. L. Holm, Benchmarking fold detection by DaliLite v.5. *Bioinformatics* **35**, 5326–5327 (2019). [doi:10.1093/bioinformatics/btz536](https://doi.org/10.1093/bioinformatics/btz536) [Medline](#)

63. H. Ashkenazy, S. Abadi, E. Martz, O. Chay, I. Mayrose, T. Pupko, N. Ben-Tal, ConSurf 2016: An improved methodology to estimate and visualize evolutionary conservation in macromolecules. *Nucleic Acids Res.* **44**, W344–W350 (2016). [doi:10.1093/nar/gkw408](https://doi.org/10.1093/nar/gkw408)
[Medline](#)